Correlation-Based Detection and Classification of Rail Wheel Defects using Air-coupled Ultrasonic Acoustic Emissions

Arash Nouri

Thesis submitted to the faculty of the Virginia Polytechnic Institute and State University in partial fulfillment of the requirements for the degree of

Master of Science

In

Mechanical Engineering

Steve C. Southward (Chair)

Mehdi Ahmadian

Reza Mirzaeifar

April, 2016

Blacksburg, VA

Keywords: Ultrasonic, Acoustics, Emissions, Health monitoring, Non-destructive test, Rail wheel, Defect detection, Features extraction

Correlation-Based Detection and Classification of Rail Wheel Defects using Air-coupled Ultrasonic Acoustic Emissions

Arash Nouri

Abstract

Defected wheels are one the major reasons for the vehicle derailment and worsen the quality of freight and passenger transportation. Therefore, timely defect detection for monitoring and detecting the state of defects is highly critical.

This thesis presents a passive non-contact acoustic structural health monitoring approach using ultrasonic acoustic emissions (UAE) to detect certain defects on different structures, as well as, classifying the type of the defect on them. The acoustic emission signals used in this study are in the ultrasonic range (18-120 kHz), which is significantly higher than the majority of the research in this area thus far. For the proposed method, an impulse excitation, such as a hammer strike, is applied to the structure. In addition, ultrasound techniques have higher sensitivity to both surface and subsurface defects, which make the defect detection more accurate. Three structures considered for this study are: 1) a longitudinal beam, 2) a lifting weight, 3) an actual rail-wheel. A longitudinal beam was used at the first step for a better understanding of physics of the ultrasound propagation from the defect, and developing a method for extracting the signature response of the defect. The inherent directionality of the ultrasound microphone increases the signal to noise ratio

(SNR) and could be useful in the noisy environments. Next, by considering the ultimate goal of the project a lifting weight was chosen, due to its similarity to a rail-wheel. A detection method and metric were developed by using the lifting weight and two type of synthetic defects were classified on this structure. Also, by using same extracted features, the same types of defects were detected and classified on an actual rail-wheel.

Acknowledgements

I owe my deepest gratitude to my advisors, Dr. Steve Southward and Dr. Mehdi Ahmadian for all of their guidance, support and endless encouragement during my master studies at the Center for Vehicle Systems and Safety (CVeSS). Their very broad knowledge and enthusiasm has greatly influenced my perception of engineering. At the same time, their intelligence and positive attitudes changed my perception of life.

I am indebted to my colleagues and friends for their big contributions to this thesis and to my research in general. I am very thankful to them for all of their technical discussions, opinions and suggestions.

I am very grateful to Dr. Reza Mirzaeifar who accept to be in my committee. I am extremely thankful for all of his guidance throughout the course of this research.

Last but not least, I would like to thank my parents, my sister, and my brothers, who made it possible for me to reach this position in my life. I am deeply thankful for their endless love, support and care.

Table of Contents

Table of Figures

List of Tables

1 INTRODUCTION

1.1 Motivation

Defective and broken wheels are among the leading causes of train derailment incidents. They also damage the infrastructure and rolling stock due to the vibrations generated by irregularities between rail and wheel contact and increase the maintenance cost. Railways require a convenient and effective inspection system to detect wheel tread damages at an early stage so that they can be repaired and incidents avoid. Recently, non-contact NDT methods have been sought to find a better way to inspect the rail wheels, to improve the railroads operating safety and accordingly reduce the maintenance cost of the infrastructure as well as service disruptions[1][2].

This research presents a two-step non-destructive method for inspecting stationary railroad wheels, based on air-coupled (non-contacting) ultrasonic acoustic emissions by exciting a wheel with a hammer strike applied radially to the wheel and measuring the resulting acoustic emissions using a portable ultrasound microphone.

The inherent directionality of the ultrasonic microphone in the selected frequency range enables good signal-to-noise ratio, allowing for measurements to be made in the presence of background noise that is commonly present in the field. As compared with other Non-Destructive Testing (NDT) methods—including the sonic (audible) range—the ultrasonic measurements have the additional advantages of having 1) higher sensitivity to both surface and subsurface defects, and 2) greater depth penetration for sub-surface flaw detection[3].

The two-step inspection process described in this study includes a first step that is intended to extract the features of each defect (commonly referred to as "baseline" measurement) that is unique for each defect, and a second step that uses the extracted features to correlate the detection of the same type of defects in other structures by defining a metric based on recognizing the similarities between each response run and the extracted signature response.

1.2 Research Objectives

The primary objectives of this study are:

- Recognizing defected structure (beam and lifting weights) from the non-defected ones in both time and frequency domain in a controlled laboratory condition by using only one ultrasonic microphone.
- Isolating the signature responses of the different type of the defects themselves.
- Develop a system for non-rolling wheels by using the various signature responses of defects, where different types of defects on a structure could be classified and detected.
- Define a metric for recognizing defected structures, which is not dependent on the location of the defect and the microphone.
- Recognizing a defected Structure that has multiple types of defects

1.3 Approach

The following approach is used to address the issues presented in this study:

- Set up a controlled laboratory setup for comparing a set of data from a defected and non–defected beams.
- Develop a MATLAB code for diagnosing the response of each specimen and comparing them.

- Develop a series of experiments for recognizing the defected lifting weight from the non–defected one.
- Isolating the defect signature response in a controlled laboratory situation and in the ideal location of the microphone with respect to the crack.
- Develop a series of experiments for lifting weight for Defected and non–defected ones. Multiple types of defects are used, and their signature responses are isolated.
- Recognize the different type/multiple types of the crack on the lifting weight

1.4 Outline

- Chapter 1 introduces the study and provides the objectives, approach, potential contributions from the research, and an outline of the dissertation.
- Chapter 2 provides the technical background for the study. The characteristics of acoustic and ultrasound , non–destructive evaluation by using ultrasound waves, Non–contact ultrasound evaluation, different couplants for ultrasounds and air couplant ultrasonic evaluation.
- Chapter 3 focuses on the details and instrumentation of beams and lifting weight experiments. It explains the details of the signals denoising procedure theory and presents the results of comparisons between defected structures vs. non–defected structures. It also includes isolating of the signature response of the defects.
- Chapter 4 discusses the theory of signal processing procedure development, as well as defining a metric for detecting defected structures and also presents the results of multiple experiments for different types of defects and microphone locations on a lifting weight.
- Chapter 5 provides the detailed results of the longitudinal beam, scaled wheel, and a real wheel

- Chapter 6 states the main conclusions of this thesis in addition to some proposed future work.

2 REVIEW ON NDT METHODS

Although most material properties characterization are gained by destructive techniques, e.g., tensile test, chemical composition analysis, metallographic determination of microstructure, etc., premature failure of structures shows the necessity of developing and applying new approaches for the future needs for recognizing this type of failure early, as well as realization of the complete life of serviceable components. Using the Non-Destructive Test (NDT) methods is one of the most applicable and innovative ways to optimize the process of the manufacturing and inspection of different components.

There are two type of NDT techniques: 1) Vibration based, and 2) acoustic based, both of which are based on the change of local impedance of defected compared to non-defected structures, due to the existence of defects [4]. Table (2-1) from [5], shows a summary of different NDT tests and their advantageous.

Table 2-1: Comparing common NDT methods

Inspection method	Parameter measured	Advantage	Disadvantage	Cost
Visual	Surface condition	Quick; modest skills required	Superficial	Low
Proof load test	Load carrying capacity	Definitive	Very slow and possibly dangerous	Very high
Coring	Specific internal dimensions	Definitive dimensions	Measurement only at test point	Moderately high

Vibration testing	Mode shapes and/or signature	Give some indirect measure of current condition	Difficult quantify data; heavily damped species give yield little response	Moderate
Impact testing	Mode shapes and/or signature	Give some indirect measure of current condition	Difficult quantify data; heavily damped species give yield little response	Moderate
Ultrasonic NDT	Wave velocities through structure	Relatively quick	Only works on individual specimens due to signal attenuation	Moderately high
Sonics	Wave velocity; tomographic cross-section	Moderately slow; gives useful information on major elements	Required skill to interpret data	Low
Conductivity	Relative conductivity	Quick; gives relative conductivities over a large area to a maximum depth of 1.5 m	Limited depth penetration of 1.5 m; complements radar	Low
Radar	Electromagnetic wave velocity	Quick; can give good penetration; can give good image of internal structure	Poor penetration through some materials; requires skill to understand data	Moderately high

As the Table (2-1) shows, one of the most versatile NDT methods is using ultrasonic waves. In this technique, detailed information about flaws or material properties of the structure could be extracted by using different wave modes. Some of the main advantages of using ultrasound NDT techniques are [6]:

- Testing can be done by using a single surface;
- Higher sensitivity to both surface and sub-surface defects;

- Greater penetration depth for sub-surface flaw detection;
- Locating and measuring the defects more accurate; and
- Compatibility for being used in automatic scanning devices.

There are two approaches for the ultrasound NDT. Contact, and non-contact methods. The contact methods have some limitation being utilized in the field and for more complex situations due to the necessity of coupling the transducer with an acoustical impedance matching a coupling medium (couplant). Using the couplant causes some problems such as, transit time errors, partial transmission and reflection of the ultrasonic energy, and changing the waveform that can lead to errors in absolute attenuation measurements, and it is one of the reason that very few reliable absolute measurements of attenuation are reported in the literature by using this approach. Oil, grease, gel, or water are usually used as the couplant for the contact ultrasound method. Another problem which this approach faces is the vibration character of the attached transducer itself, which can influence the receiving ultrasound as well, because of the transducer vibrational mode shape with corresponding frequency, amplitude, and directional responses, as well as loading the surface, attached and modify the receiving signals [7]. Figure 2-1 illustrates the different methods of ultrasonic methods.

On the other hand, there are non-contact methods, which the most common non-contact ultrasonic techniques are electromagnetic acoustic transducers (EMATs), laser beam optical generators and detectors, and the most recent one, air (gas) coupled methods. EMATs method is frequently using for defect characterization, particularly in metal bars, tubes, pipes, and plates. The biggest problem of EMATs is the significant decrease in efficiency of the ultrasound generation and detection with decreasing distance between the EMATs sensor face and the test surface, as well as its limitation to be only used for the electrically conducting materials. The next general non-contact method is

using laser ultrasound that can be utilized as NDT method for both conducting and non-conducting materials [7].

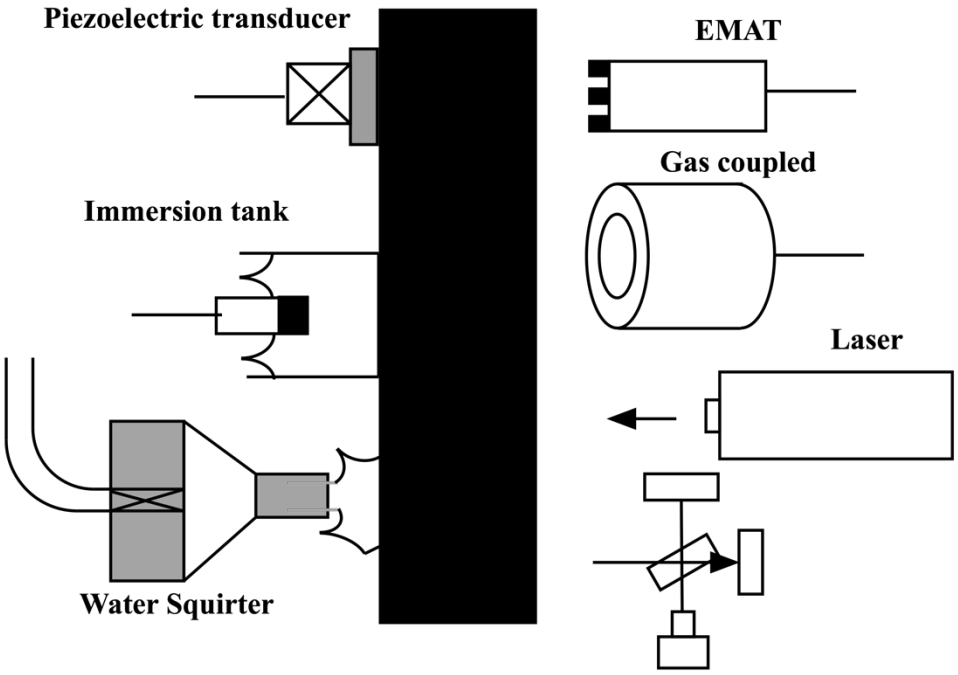

Figure 2-1: Contact and non-contact ultrasonic techniques

Air(gas)-coupled ultrasound is a relatively new technique, used in the industry shown to be very efficient and fast for testing, and also, could be used for detecting the subsurface defects. Although this method is quick and efficient, it needs a professional operator for recognizing the defect and work with the taken runs.

Today one of the greatest problems of the rail industry is the inspection of the tracks and wheels. Although many varieties of inspection methods have been used, none of these methods are not satisfactory for detection of many possible defects. A wide range of techniques from simple visual inspection to magnetic induction and water-coupled ultrasonic were used previously. Using the

water coupled ultrasonic, is one of the most effective and efficient methods, but it very expensive and needs an elaborate and expensive facilities [7].

One of the most challenging parts in non-contact ultrasonic techniques is extracting the data from the noisy signals that endangered test quality and repeatability [8], which mostly related to lack of any advanced signal processing software to process and detect signals [9]. There are two types of noise sources in the ultrasonic signals, Acoustic and non-acoustic. Acoustic noise is caused due to the property of the material and random vibration or mode summation due to input. The amplitude and arrival time of acoustic noise are random for each signal causing an either false defect response or mask the defects [8].

Another source of the noise is non-acoustic disturbances. This type of noise is called instrumental noise, which derived from the stochastic disturbance in the semiconductor element of the electrical circuit. The most commonly encountered electrical noise is white noise, which has a flat power spectrum and it is considered that different measurements are non-correlated, so signal averaging can eliminate this noise [8][10].

The next challenge after de-noising the signals is to detect the response of the defect in them. One of the most efficient methods to find the similarity between two signals is convolution based methods [11], [12]. These methods have been used extensively for pattern recognition problem such as face detection, object recognition, and industrial inspections [12]–[15]. Also, defining a metric is necessary to define how much similarity is found by convolution based method, which in most cases, it was defined as finding the most sharp peak in the convolution results [11].

3 EXPERIMENTAL SETUP AND APPARATUES

3.1 Apparatus

3.1.1 Ultrasonic Sensor

Avisoft Bioacoustic's CM-16 (Figure 3-1) was used as an ultrasonic sensor for this research. This microphone has a bandwidth of up to 150 kHz (Figure 3-2) that goes well into the ultrasonic range.

Figure 3-1: Avisoft Bioacoustic CM-16 (© Avisoft Bioacoustic)

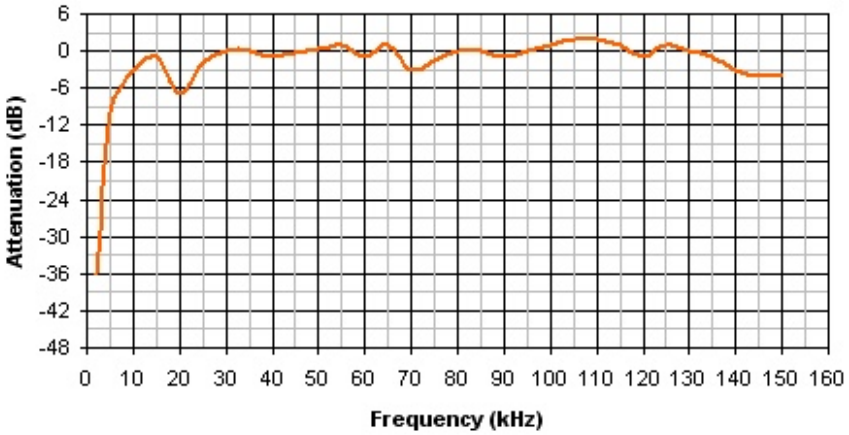

Figure 3-2: Frequency Response of of Avisoft Bioacoustic CM-16 (© Avisoft Bioacoustic)

The ultrasound sensor is directional, which in noisy environments is desirable and can help to isolate the acoustics waves. Thus, it could focus only on the target direction, and by increasing its relative angle with the target, the energy, absorbed by the microphone in higher frequencies is reduced, as can be seen in the microphone polar diagram (Figure 3-3)[16].

Table 3-1: Specifications of Ultrasound Sensor[16]

Frequency Range	10 kHz – 200 kHz
Approximate Input – Referred self – Noise Level	18 dB SPL
Power Supply	5 V, 30 mA
Approximate Sensitivity	50 mV/Pa
Maximum Differential Output Voltage Swing	±5 V
Connector	Male XLR-4 Socket
Dimensions	36 × 36 × 125 mm
Weight	150 g

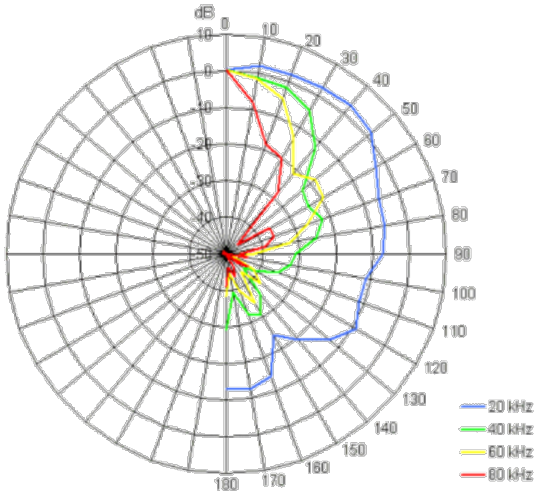

Figure 3-3: Polar diagram of the ultrasonic sensor directionality (© Avisoft Bioacoustic)

3.1.2 Data Acquisition System (DAQ)

The selected ultrasonic sensor with the bandwidth of 150 kHz. Based on Nyquist theorem, to use the maximum bandwidth of the sensor using a DAQ system with a two times larger sampling frequency or larger is needed.

Due to its availability in our lab, Tektronix TDS 3014B was used as the DAQ system with a maximum sampling rate of 1.25 GS/s per channel, and bandwidth of 100 MHz. It also provided four channels allowing for additional sensors to be used during testing. Furthermore, Tektronix TDS 3014B include a scope that allowed seeing the captured data simultaneously before storing it directly on a floppy disk or computer. The sampling frequency for all of the experiment was 5 MHz.

3.2 Synthesized Defects

For developing and validation any new NDT methods, the necessity of having different types of defects is inescapable. Also, the preference is to have a structure with only one type of defect at a time. Finding a non-defected structure or a structure with a specific type of the defect is difficult so, synthesized defects were used for the experiment. Exciting any defects on the structure changes its vibration characteristics, or it could be said that it changes the stiffness, mass or energy dissipation properties of the structure [17]–[19]. Thus, defects were synthesized in every structure in this research by using the same concept.

3.2.1 Synthesizing Defects on Beam

For synthesizing the defect in a beam, two aluminum beams were connected to each other by using two bolts and bridge (Figure 3-4). In this situation, gravity makes the edges of the two beams closer to each to simulate a real defect.

The ultrasound emissions were created as the pressure wave passed through the cracks, due to the mechanical interface. In addition, the resonance of the vibration of another part of material around the defected area could cause nonlinear resonance when elastic waves interact with defects [20], [21].

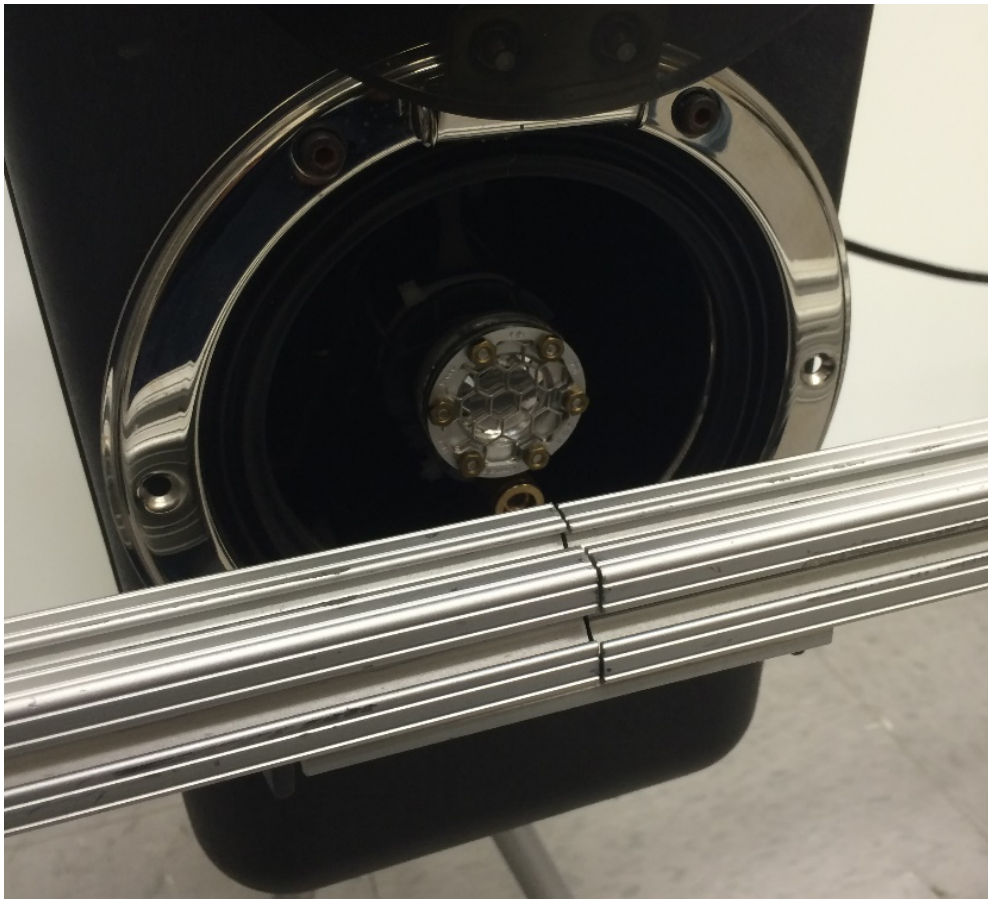

Figure 3-4: Synthesizing defect by using two beams and a standard bridge

In order to create different defects on beam, some materials, like plastic and paper, were added to the interface of the defect to change the stiffness of the defect.

3.2.2 Synthesizing Defects on Lifting weight and Rail-Wheel

The defects were synthesized on the wheel by changing the mass using two pairs of magnets (Figure 3-5). The first defects (a) were created by using a pair of the ceramic magnets with the

weight of 3.35 oz., and the second defects (b) were synthesized by using a pair of the neodymium magnets with the weight of 0.63 oz.

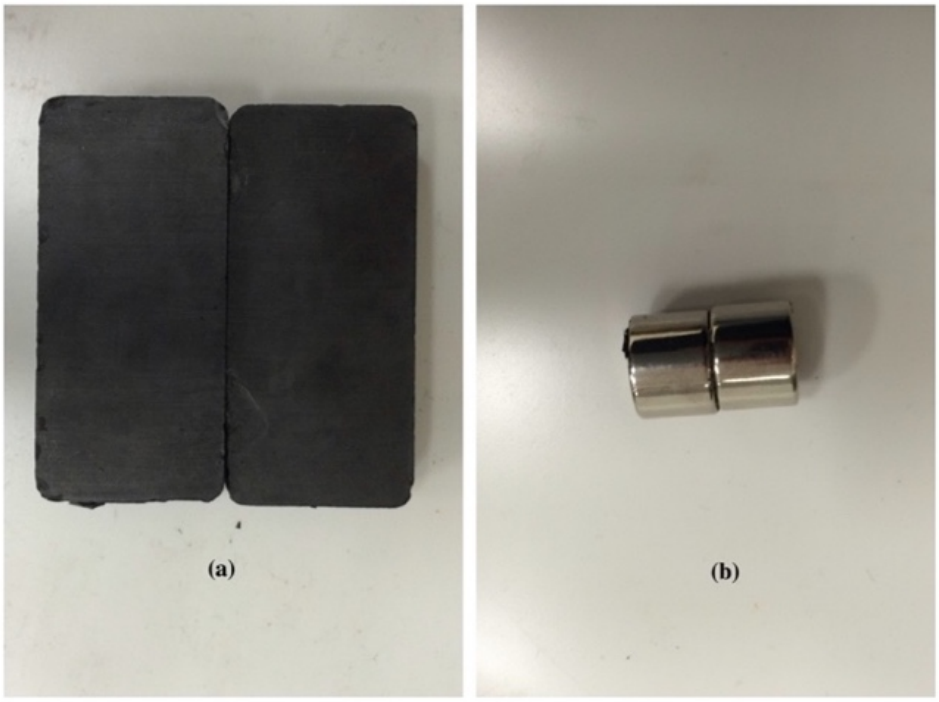

Figure 3-5: a) Synthetic defect #1 b) Synthetic defect #2

3.3 Experimental Setup for Longitudinal Beam

As the first attempt to better understand the wave propagation, two aluminum beams were used for creating a defected beam by connecting to each other by using two bolts and a bridge. The ultrasonic microphone can detect emissions from defects; however, the emissions do not always contain signature responses of defects. Thus, it is important that the wave propagation through the beam be understood.

This experiment is a study of the ultrasonic response of the both non–defected and defected beams (Figure 3-6). Beams are aluminum 8020, and their length of the both beams are 2.24 ft.

The non–defected beam is an integrated beam of length 2.24 ft., but the defected beam consists of two non–defected beams, which have the same length (1.12 ft. each). As mentioned earlier, for this study the crack was synthesized, because it is hard to have a structure with only one type of defect. A hammer was used to excite the structure. The impact site for all runs is the same, and all impacts have approximately the same energy level.

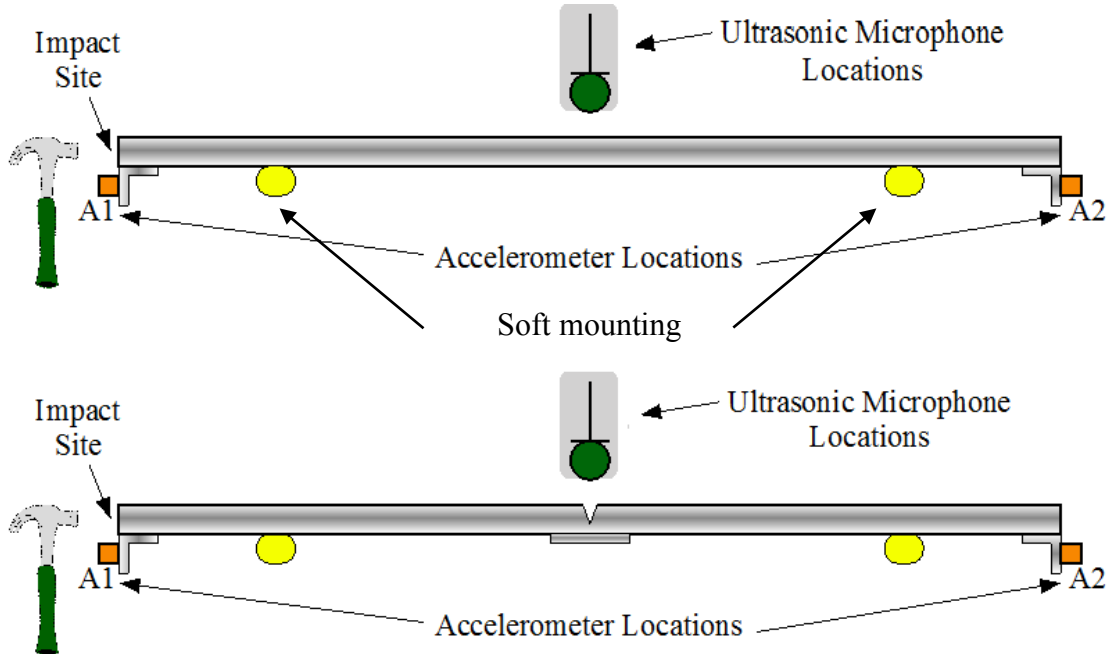

Figure 3-6: Illustration for the experimental setup and location of the ultrasound microphone

3.4 Experimental Setup for Lifting-Weight

The primary goal of this project was to find the defects on the rail-wheel, so after finding defects on the beam, the goal was to find defects in such a more similar structure to a rail-wheel. Thus, a lifting weight of cast iron was used as a scaled wheel model for this study with 12 in diameter and 25 lb weight.

An experimental setup was designed by defining two locations for microphone and defects (Figure 3-8). The ultrasonic microphone was located 1 in away from the structure radially, and another position located 7 in away from the structure axially. That these locations were named radial and axial locations respectively. In fact, the radial location was used as the calibrating location, used for extracting defects signature responses, and the axial location was the validating location for detecting the same type of defect.

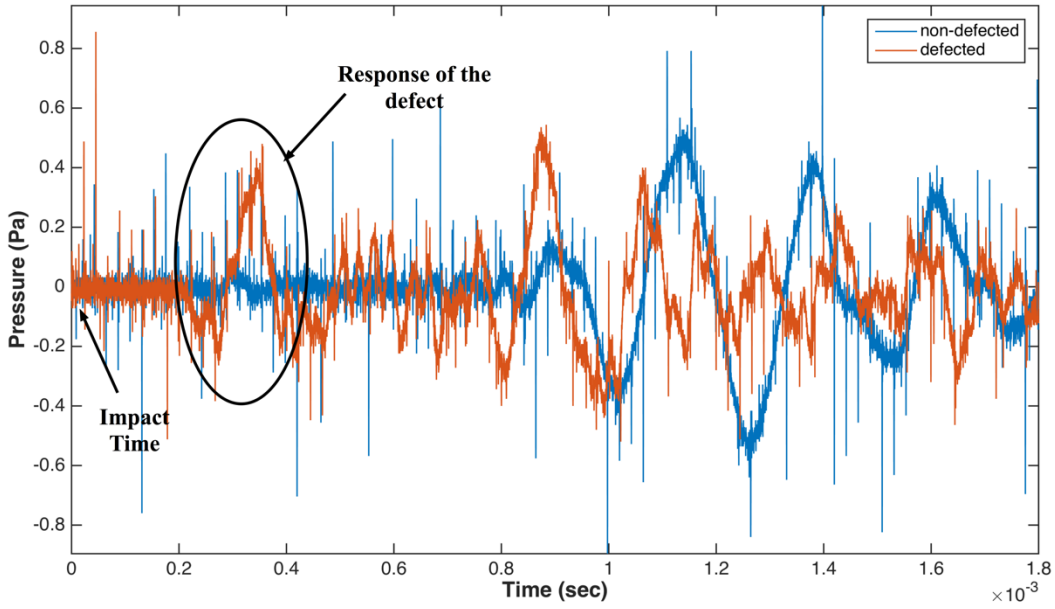

Figure 3-7: Typical time series data for the defected beam

Defects were placed once in 0˚, and another in 90˚ relative to the radial location of the microphone. Also, as mentioned earlier two types of synthesized defect were used on the wheel as defects.

Four experiments were considered here for isolating the signature response of defects as well as detecting them: 1) Microphone was located at the radial location without any defect present, 2) Microphone was located at the radial location, and defects were at 0˚, 3) Microphone was at radial location and defects were at 90˚, 4) Microphone was at axial position and defects were at 90˚. An

impulsive input energy was applied radially to the wheel for exciting on the opposite side of the wheel. The sampling frequency was 5 MHz for this experiment.

Figure 3-11, illustrates a sample of a pre-processed data for this experiment.

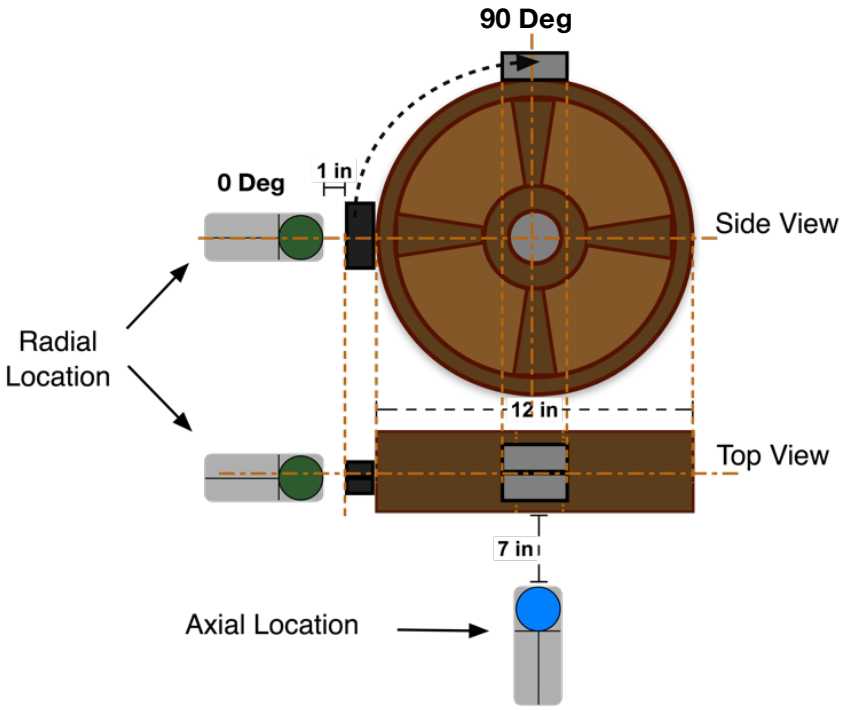

Figure 3-8: Illustration of experimental setup focused on lifting weight with synthetic defect

Figure 3-9: One of the experimental setups. Microphone at the radial location and the defect at 0 degrees

Figure 3-10: One of the experimental setups. Microphone at the axial location and the defect at 90 degrees

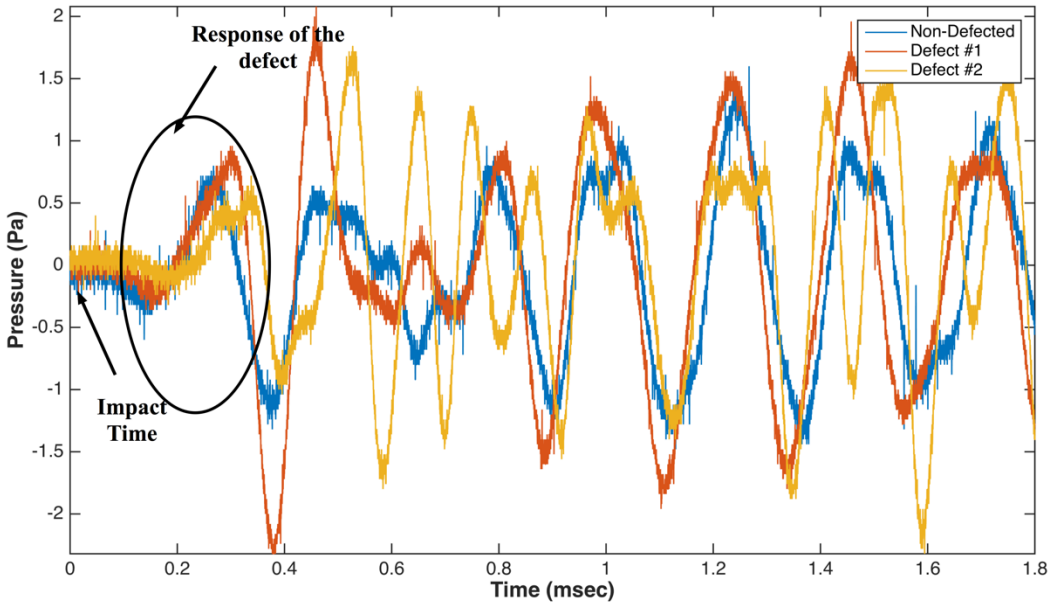

Figure 3-11: Typical time series data for the lifting weight

3.5 Experimental Setup for Rail-Wheel

The same Synthetic defects and experimental setup were used for the actual rail-wheel. The experiment was done in Norfolk Southern (NS) facility at Roanoke, VA, and one defected and a non-defected wheel were used. A wheelset was provided by NS, with one non-defected and one defected wheel. The microphone was placed in opposite side of the wheel for each setup; also, the Hammer input used as the excitation. Three setups were considered for this experiment. In first experimental setup (Figure 3-12), the defects were synthesized on the non-defected wheel on the both 0 and 90 degrees location. In the second experimental setup, the experiment was repeated on the wheel with actual defects (3-13), which the defects were almost in the same location at 0 and 90 degrees. The third experimental setup was on the wheel with the actual defect as well as attaching the synthesized defects on that at 90 degrees (Figure 3-14). The last setup was on the detected wheel that the other defect of the wheel was hidden by rolling the wheel and out the defect

on the contact patch of the wheel and the rail. Figure (3-15) shows a typical setup for the experiment for the actual wheel.

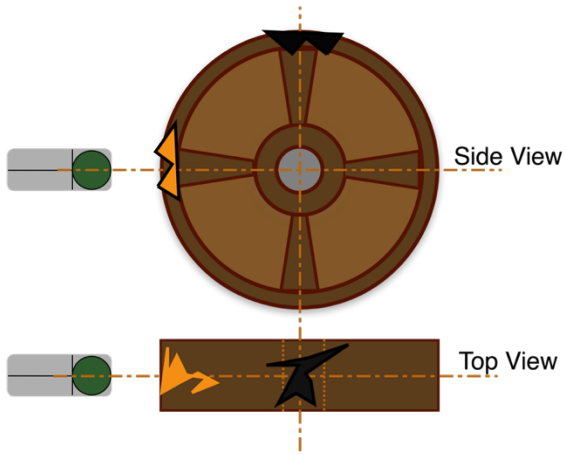

Figure 3-12: Experimental setup for wheel with actual defects

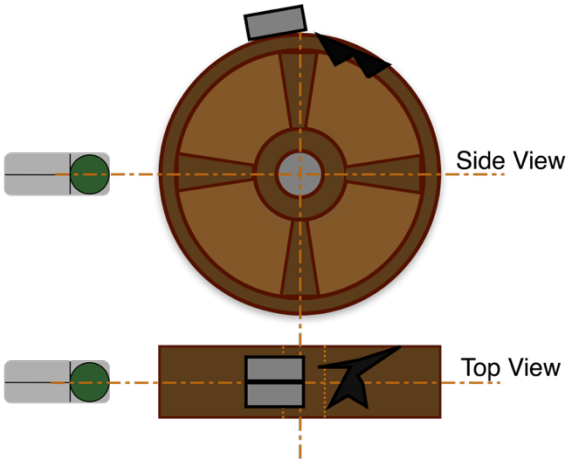

Figure 3-13: Experimental setup for a wheel with the both synthetic and actual defects

Figure 3-15 shows an example run of this experimental setup.

Figure 3-14: Actual rail-wheel experimental setup

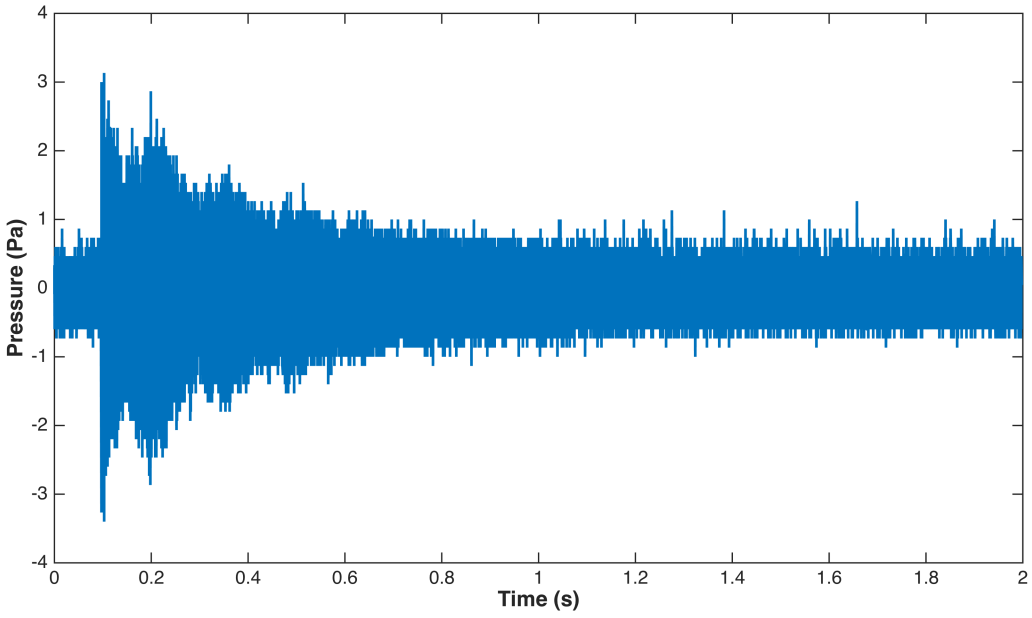

Figure 3-15: Typical impact response of the lifting weight in time domain

4 ISOLATION OF EACH DEFECT SIGNATURE RESPONSES

As mentioned earlier the first part of this study focused on extracting the response of a defect, but results from a large number of test runs indicated that the acquired data tends to be noisy, which made it difficult to extract the signature response of defects. By analyzing the runs, noise was classified into two classes; Out-of-Band, and In-Band noise. Then, a semi-automatic procedure was developed using MATLAB to eliminate the influence of noises and extract the repeatable response of each defect, which is referred to as signature response of the defect. Following shows the steps for de-noising procedure:

- Band-pass filter each response run over a pertinent frequency range for that particular defect
- Normalize all the runs by their powers
- Estimate the relative time shifts between all calibration responses based on mutual correlation
- Select a reference run which has the smallest average time shift with respect to all other calibration responses
- Prune response runs with excessive time shifts relative to the selected reference
- Numerically shift all remaining runs relative to the reference, i.e. re-align signals in the time domain
- Perform time-domain averaging of the processed calibration responses to generate a de-noised defect signature

4.1 Eliminate Out of Band Noises

Generally, they were two types of noise in all of the runs, out-of-band and in-band noise. Equation (4-1) shows each run consists of the signature response of the defect, plus the in-band and out-of-band noise [22]

$$U_{raw}(t) = U_{Sig}(t) + U_{inband}(t) + U_{oob}(t) \quad 4\text{-}1$$

where, $U_{Sig}(t)$ is the signature response of the defect, $U_{inband}(t)$ is the in-band noise, and $U_{oob}(t)$ is the out –of-band noise. The out-of-band noise is the noise that exists in the frequency bandwidth that is not desirable for the analyses. Thus, for extracting different defect signature, it is not necessary to consider all the available frequency range. This type of noise was eliminated by using a band-pass filter. The desirable frequency range was determined by comparing the response of defected structure with the response of the non-defected structure as well as the noise floor in the frequency domain for each synthesized defect (Figures 4-1 to 4-3). Also, the frequency ranges out of the apparatuses range (under 15kHz, and higher 170kHz) should be eliminated as well.

A 4^{th} order Butterworth band-pass filter is defined to eliminate out-of-band noise. All runs were band-pass filtered, and the break frequency for high and low pass filtering are in Table (4-1). As mentioned earlier these frequency ranges were detected by looking at the PSD plots (Figures 4-1 to 4-3) for each defect.

Table 4-1: Used break frequencies fro each structure and defect

Defect	Low-pass break frequency (kHz)	High-pass break frequency (kHz)
Longitudinal beam	25	45

Lifting weight with Synthesized defect #1	18	60
Lifting weight with Synthesized defect #2	20	45

After this step, all the out-of –band noise was eliminated and as the equation (4-2) shows, each run only consists of the signature response and in-band noise.

$$U_{filt}(t) = U_{Sig}(t) + U_{inband}(t) \qquad 4\text{-}2$$

Figure 4-1 shows an example of data after and before filtering. In this picture, the time axis scaled such as t = 0 is the time of the impact.

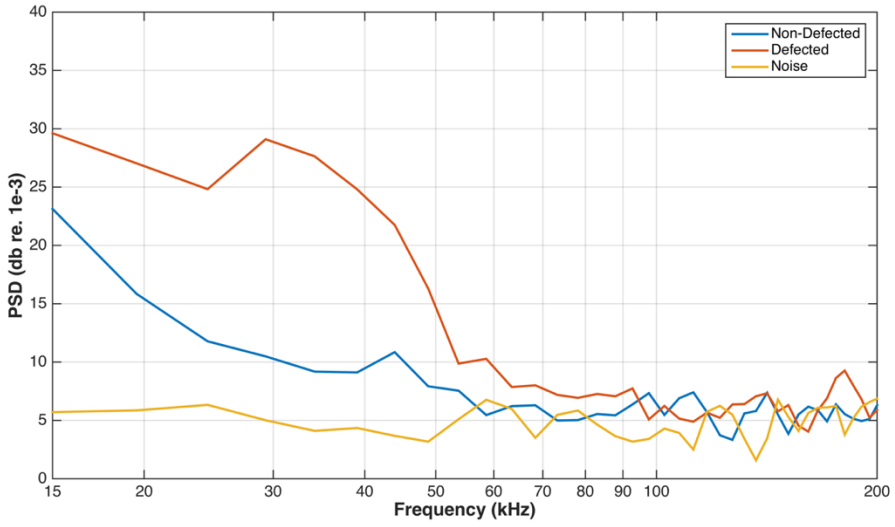

Figure 4-1: Power spectrum density of the defected and non-defected longitudinal beams

As the Figure 4-4 shows, although, there were a lot of data that have been eliminated from the raw data, due to the PSD plots of defects (Figures 4-1 to 4-3) these data do not include any data from the defect.

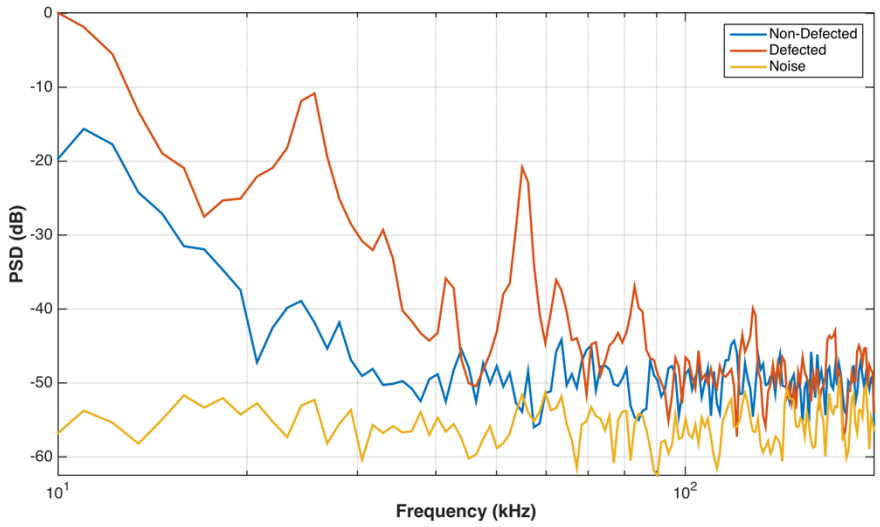

Figure 4-2: Power spectrum density of the defected and non-defected longitudinal lifting weight with synthesized defect #1

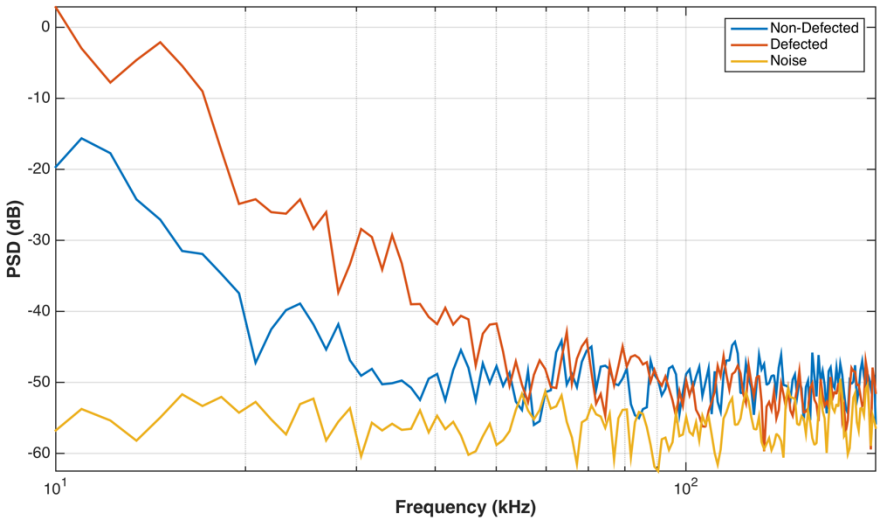

Figure 4-3: Power spectrum density of the defected and non-defected longitudinal lifting weight with synthesized defect #2

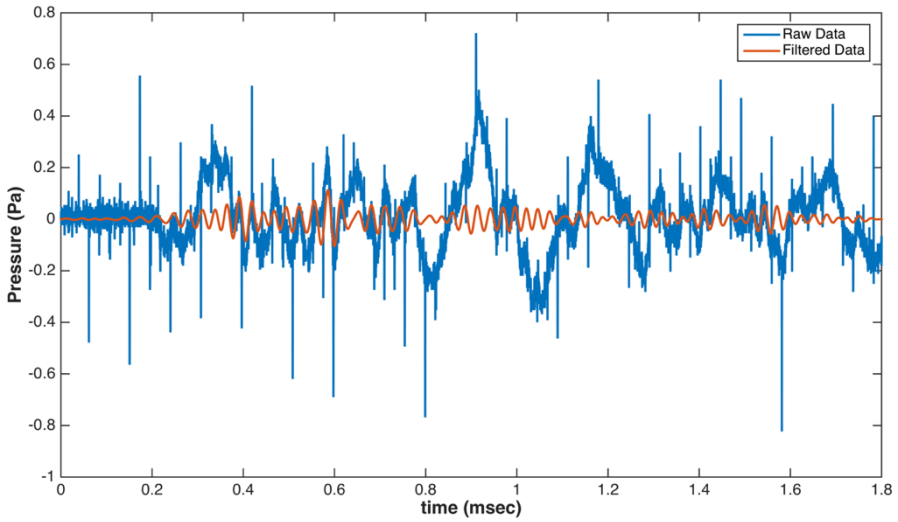

Figure 4-4: Example of the longitudinal beam run after and before filtering

4.2 Normalize Amplitude of each Response

As mentioned earlier beside the out-of-band noises there are in-band noises as well. To eliminate these noises; time domain averaging was used to reduce the noise. Each signal consists of the signature response or primary response of defects plus noise that these noise have independent sources than the signature response of the defect. Thus, by doing the averaging in the time domain, the amplitude of this noise should decrease and give a clearer response to the signature of the defect [22].

Due to the difference in input for each experimental run, for applying the time-averaging method, all the raw data should be scaled with respect to their input energies. The power of each run was used as a scaling factor to scale each run that is equal to the standard deviation of each run [23].

$$U^n_{scaled}(t) = \frac{U^n_{filt}(t)}{\sigma_{U^n_{filt}(t)}} \qquad 4\text{-}3$$

where σ is the standard deviation of each filtered run. In other words, after the scaling, all runs should have the same amount of power

$$\sigma_{U^i_{scaled}(t)} = \sigma_{U^j_{scaled}(t)} \quad \forall\, i,j \tag{4-4}$$

Figure (4-5) shows two runs before and after the scaling.

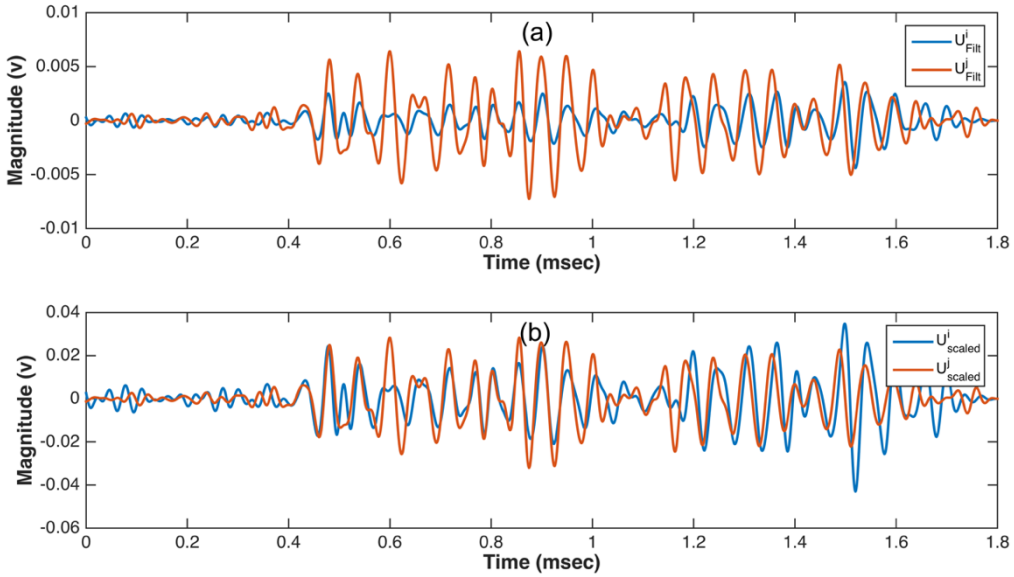

Figure 4-5: Comparing two runs after and before the scaling process

4.3 Estimate the Relative Time-Shift Between all Calibrated Responses

For applying the time domain averaging on the runs, it is important that the data be aligned as well as possible. The DAQ system used in this experiment, was triggered respect an accelerometer, which was located at the location of the input. Due to the reason that the location and the energy of each hammer hit was different from another, the triggering was not constant for all the runs. The relative lags for each signal were calculated about all the signals by finding the relative lag shift of the peak of the cross-correlation of each signal with respect to all other signals [22]. Assume two signals U_1, and U_1

$$U^i_{scaled}(t) = U^i_{sig}(t + \Delta_i) + U^i_{inband}(t) \quad \text{4-5a}$$

$$U^j_{scaled}(t) = U^i_{sig}(t + \Delta_j) + U^j_{inband}(t) \quad \text{4-5b}$$

where, $U^i_{scaled}(t)$ and $U^j_{scaled}(t)$ are two separate scaled runs from a defected structure, U^i_{sig} is the signature response of a defect. Both $U^i_{inband}(t)$, and $U^j_{inband}(t)$ are noise, which does not have any correlation with U^i_{sig}. Δ_i and $\Delta_j$are the delay for each run.

One method for calculating the error between two runs is to compute the cross-correlation function between $U^i_{scaled}(t)$, and $U^j_{scaled}(t)$ [22] [24].

$$\rho_{U^i_{scaled}(t)U^j_{scaled}}(\tau) = \mathrm{E}\left[U^i_{scaled}(t)U^j_{scaled}(t-\tau)\right] \quad \text{4-6}$$

where, E denotes expectations and ρ presents the cross-correlation operation. By expanding the above equation

$$\begin{aligned}\rho_{U^i_{scaled}(t)U^j_{scaled}}(\tau) &= \mathrm{E}\left[U^i_{scaled}(t)U^j_{scaled}(t-\tau)\right] \\ &= E\left[U^i_{sig}(t+\Delta_i)U^j_{sig}\left(t+\Delta_j\right)\right] + E\left[U^i_{sig}(t+\Delta_i)U^j_{inband}(t)\right] \\ &+ E\left[U^i_{sig}(t+\Delta_i)U^i_{inband}(t)\right] + E\left[U^i_{inband}(t)U^j_{inband}(t)\right]\end{aligned} \quad \text{4-7}$$

Where the expected value of the signature with in-band noises is zero, because there is no correlation between the signature response of the defect and noise, also by applying high-pass Butterworth filter, the noise were forced to have zero mean.

$$\begin{aligned}\rho_{U^i_{scaled}(t)U^j_{scaled}}(\tau) &= \mathrm{E}\left[U^i_{scaled}(t)U^j_{scaled}(t-\tau)\right] \\ &= E\left[U^i_{sig}(t+\Delta_i)U^j_{sig}\left(t+\Delta_j\right)\right] + 0 + 0 + 0\end{aligned} \quad \text{4-8}$$

$\Delta_{i.j}$ was defined as the time shifting error between U^i_{scaled} and U^j_{scaled}, and defined as the value of τ that maximizes the absolute value of $\rho_{U^i_{scaled}(t)U^j_{scaled}}(\tau)$

$$\Delta_{i.j} = \arg_t \left(\max \left(\left|\rho_{U^i_{scaled}(t)U^j_{scaled}}(\tau)\right|\right)\right) \quad 4\text{-}9$$

Figure 4-6 shows the relative time shifting error between two example runs in time domain and their relative delay with respect to each other, after calculating their cross-correlation.

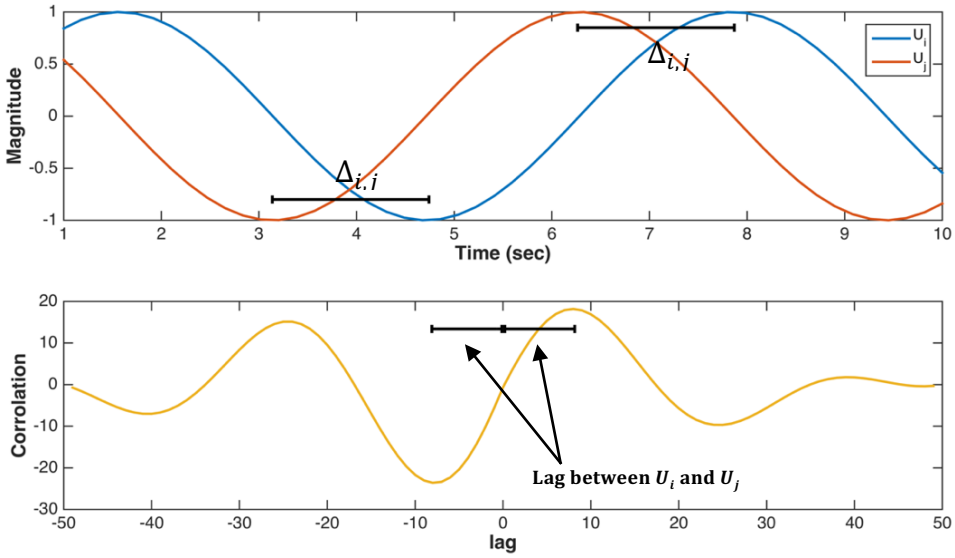

Figure 4-6: Example of the delay between two runs in defected longitudinal beam

Thus, the time shifting error was calculated for all of the runs for both of the lifting weight and the longitudinal beam and illustrated by using a pixel plot in Figure 4-7 to 4-9.

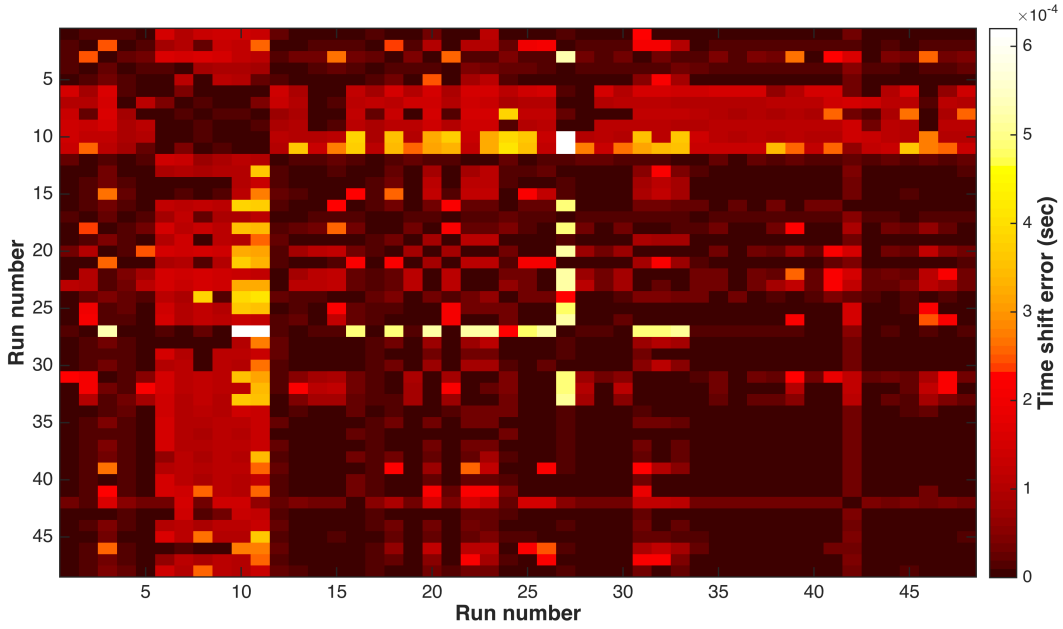

Figure 4-7:Time-shifting error of each run with respect to all the other runs for the longitudinal beam

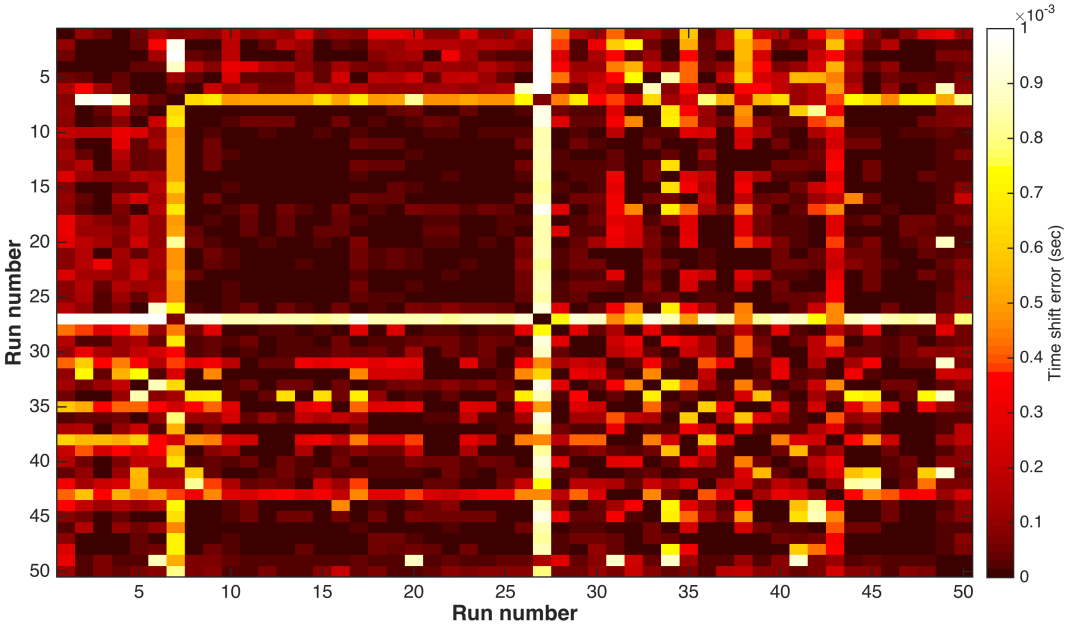

Figure 4-8: Time-shifting error of the each run with respect to all the other runs for the lifting weight with synthesized defect #1

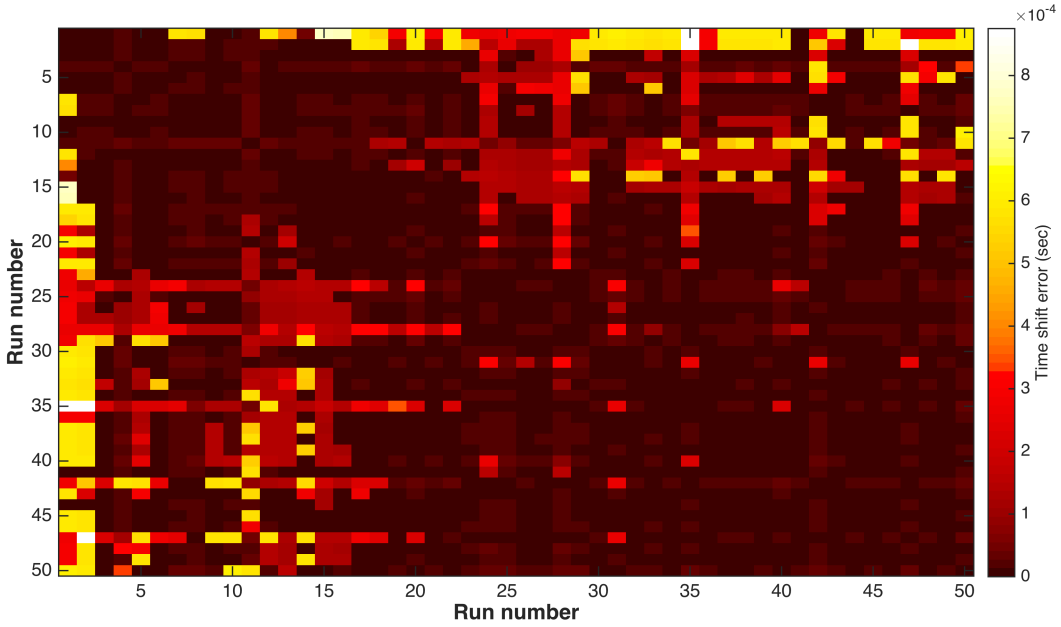

Figure 4-9: Time-shifting error of the each run with respect to all the other runs for the lifting weight with synthesized defect #2

4.4 Select a Reference Run for Shifting all runs

In the next step, the average of the relative time shifts between each run with respect to the other runs was calculated (Equation (4-10)).

$$\bar{\Delta}_i = \left(\frac{1}{N}\right)\sum_{i=1}^{N}\Delta_i \qquad 4\text{-}10$$

where, N is the total number of runs, and Δ_i is all relative shifting error of a individual run with respect to all other runs. The run with the least amount of the average time-shifting $\bar{\Delta}_i$ was chosen as the reference run and all other runs were shifted relative to it. Figures 4-10 to 4-12 illustrates the average time shift error for each structure and defect.

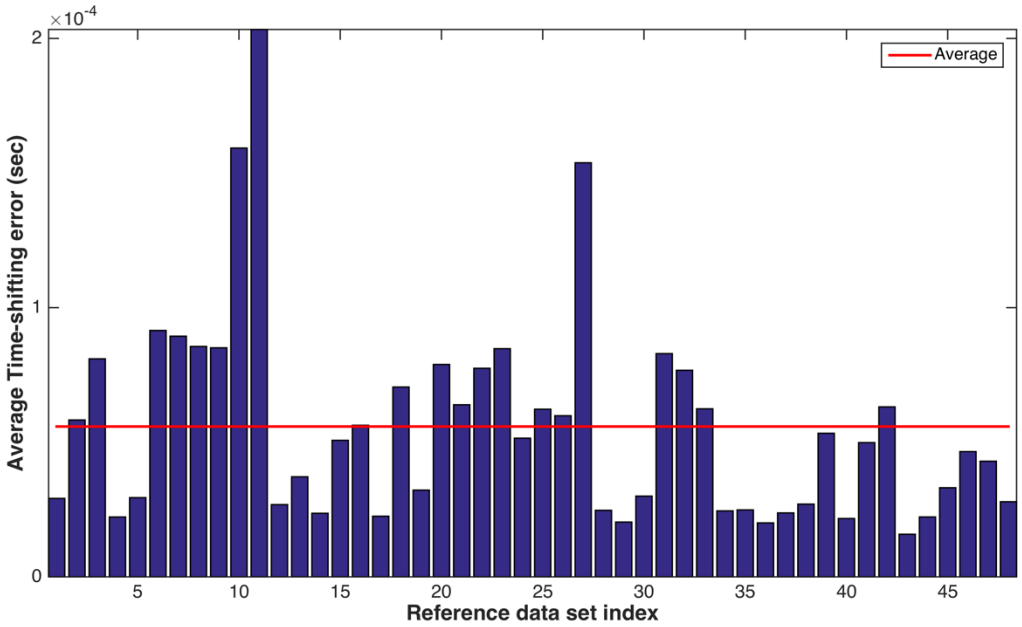

Figure 4-10:Average time-shifting error for the longitudinal beam

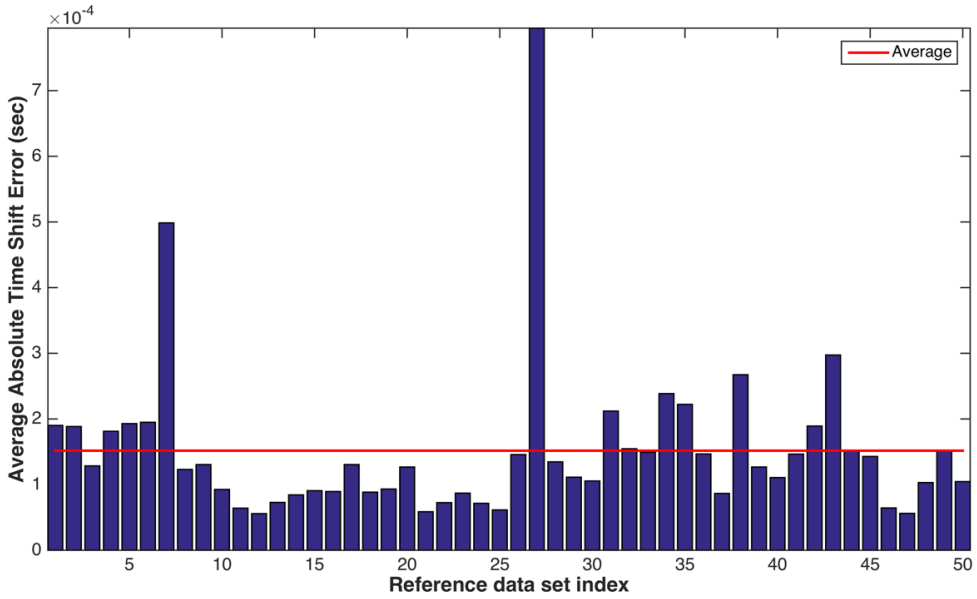

Figure 4-11: Average time-shifting error for the lifting weight with synthesized defect #1

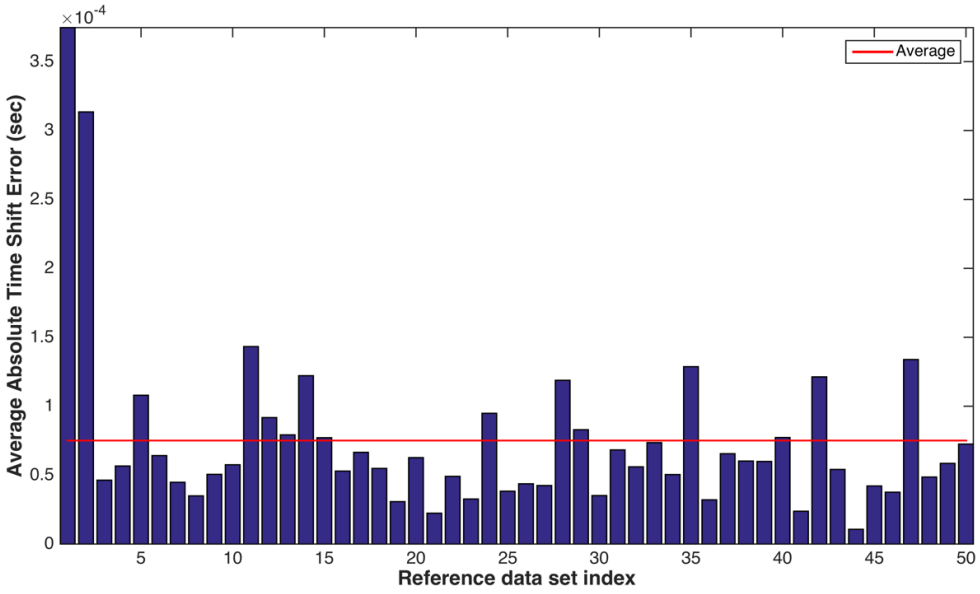

Figure 4-12: Average time-shifting error for the lifting weight with synthesized defect #2

4.5 Re-align Remaining Runs in Time-Domain

As mentioned before in order to reduce their time shifting error with respect to each other, or re-aligning them a reference runs from was chosen, and all other runs were shifted with respect to the reference run (Equation 4-11). Figure 4-13 shows an example for comparing two runs before and after the re-aligning.

$$U^i_{shift}(t) = U^i_{scaled}(t + \Delta_{i,j}) \qquad 4\text{-}11$$

For re-aligning runs, a piecewise cubic Hermite interpolation polynomial method was used. This approach used the interpolation between each two points and preserves monotonicity and the shape of the data. But, at the end and starting point of the data, where there is no other point exist before or after that, the shifted data would be deformed. To prevent that, a time domain envelope was defined (Figure 4-14) to clamp the starting and ending of each data (Equation (4-12)). During the

experiment, a 10% timing trigger threshold was set in the DAQ, also all the signature has appeared in the middle or initial time of each runs. Thus, decreasing the magnitude of each run at these times will not eliminate any data.

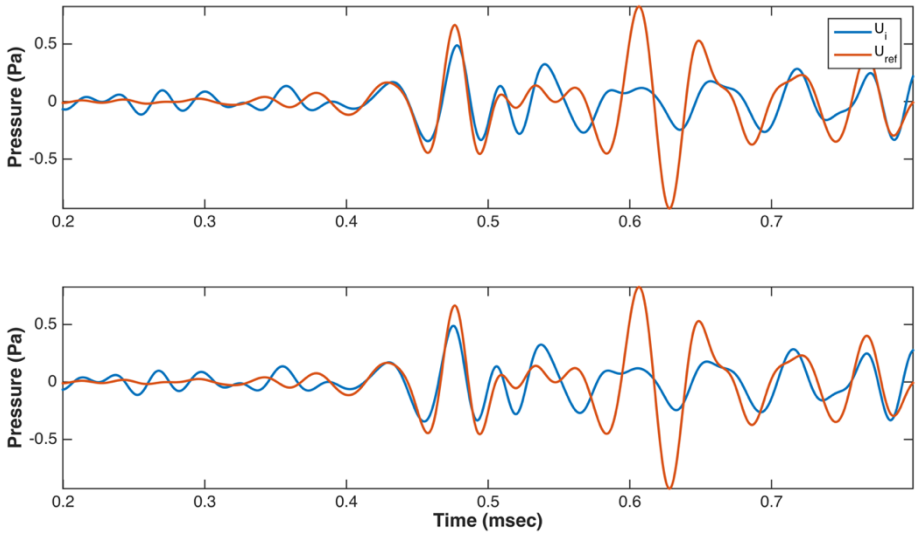

Figure 4-13:Comparing two experimental runs before and after the re-aligning procedure

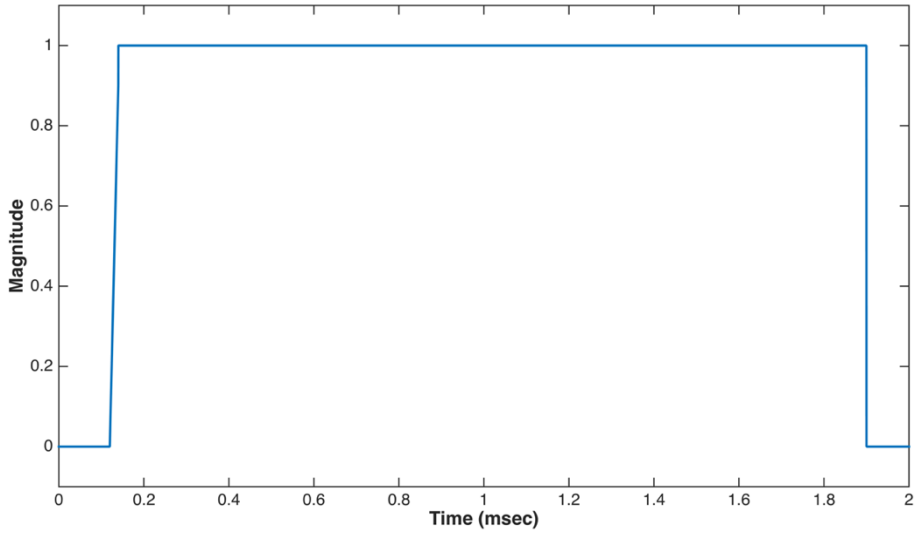

Figure 4-14: Time domain envelope used after the shifting process

$$U^i_{env}(t) = W(t)U^i_{shift}(t) \qquad 4\text{-}12$$

where $W(t)$ is the defined envelope, and $U_{shift}^{i}(t)$ is an individual shifted run.

4.6 Prune Response Runs with Excessive Relative Time-Shift

After shifting all the runs, the average relative time-shift of all runs were calculated again that it was shown in Equation (4-13).

$$\bar{\delta}_i = \left(\frac{1}{N}\right)\sum_{i=1}^{N} \delta_i \qquad 4\text{-}13$$

where N is the total number of runs, and δ_i is the new calculated relative time-shift error after the initial shifting in time domain. By re-aligning the runs the time shifting error between each two runs should be reduced significantly

$$0 \leq \left|\delta_i - \delta_j\right| \ll \left|\Delta_i - \Delta_j\right| \qquad 4\text{-}14$$

In the lifting weight experiment the time shifting errors after the shifting were reduced significantly but in the longitudinal beam, this reduction was not as much. Although in some cases like the longitudinal, re-aligning did not have any significant effect on the error, still it is one of the steps that reduced the error and help to improve the runs the time-domain averaging.

At this point, runs which still have a meaningful amount of the time–shifting error should be eliminated. Thus, a metric was needed to define to prune these type of runs, which still have a significant amount of time-shifting error. By considering the average time-shifting error as a statistical metric, the outliers could be recognized and eliminate quickly[25]. Outliers are defined

as the data that lies outside the distribution and the pattern of the rest of the data [26]. Thus, a Pruning Margin (PM) was defined for recognizing the outliers as Equation (4-15), and data with the error more than the pruning Margin were pruned. Equation (4-15) shows the defined metric for this study. In addition, sorted values of average time shifting error, it is obvious that this pruning margined works well (Figure 4-15 to 4-17).

$$PM = \bar{\delta} + 1.4 \times \bar{\sigma} \tag{4-15}$$

where, $\bar{\delta}$ is the mean value of average time shifting after the re-aligning (Equation 4-17), and $\bar{\sigma}$ is the standard deviation of average time shift error for all re-aligned runs (Equation 4-18).

$$\bar{\delta} = \left(\frac{1}{N}\right) \sum_{i=1}^{N} \bar{\delta}_i \tag{4-16}$$

$$\bar{\sigma} = \left(\frac{1}{N}\right) \sum_{i=1}^{N} \left(\bar{\delta}_i - \bar{\delta}\right)^2 \tag{4-17}$$

Figure 4-15 to 4-17, shows the sorted average time shifting error after the re-aligning process for all the runs, as well as the average of them and the metric values for each case.

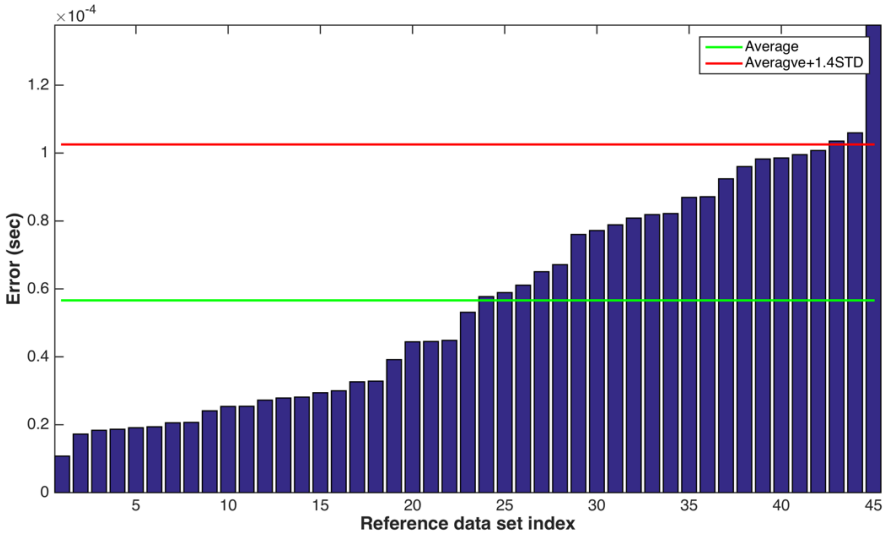

Figure 4-15: Sorted average time shifting error after the re-aligning for the longitudinal beam

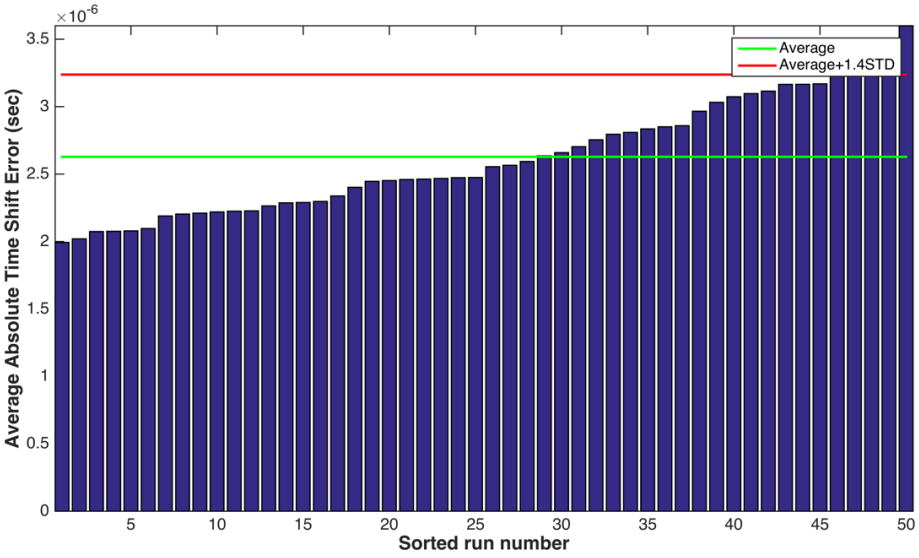

Figure 4-16: Sorted average time shifting error after the re-aligning for the lifting weight with synthesized defect #1

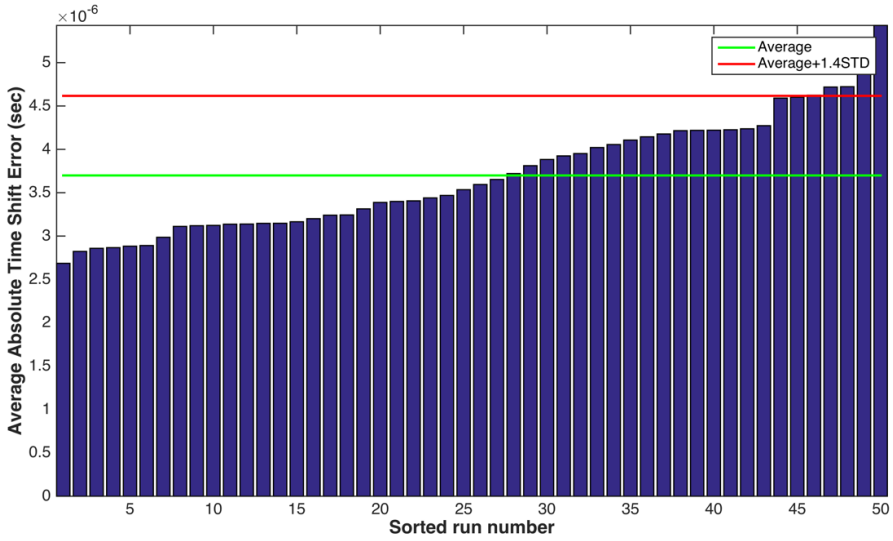

Figure 4-17: Sorted average time shifting error after the re-aligning for the lifting weight with synthesized defect #2

4.7 Time Domain Averaging

As mentioned earlier, it was decided that in-band random noise could be reduced by averaging multiple runs in the time domain. Thus, multiple runs were taken from the same experimental setup, were scaled by their powers, and shifted in the time domain. In the final step, the average of these runs was calculated (Figure 4-18 4-20). Equation (4-18) shows the estimated value for the signature response of the defect. Although most of the in-band noise were eliminated, it still has some amount of noise in it.

$$\widehat{U}_{sig}^{n}(t) = \left(\frac{1}{N}\right)\sum_{i=1}^{N} U_{env}^{i}(t+\delta_i) + U_{inband}^{i}(t) \qquad 4\text{-}18$$

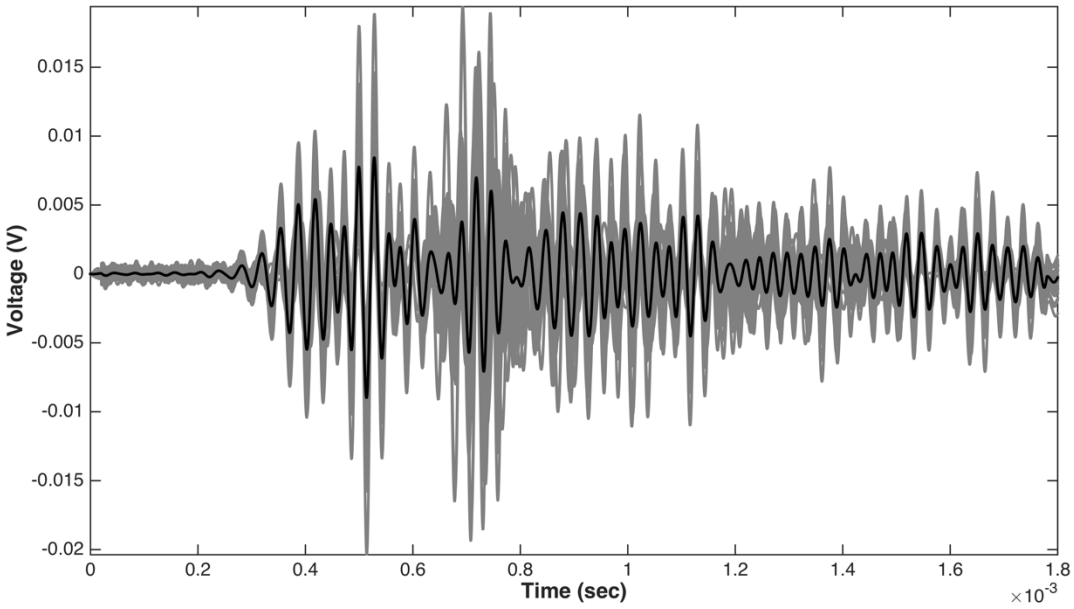

Figure 4-18: Signature response of the defected beam

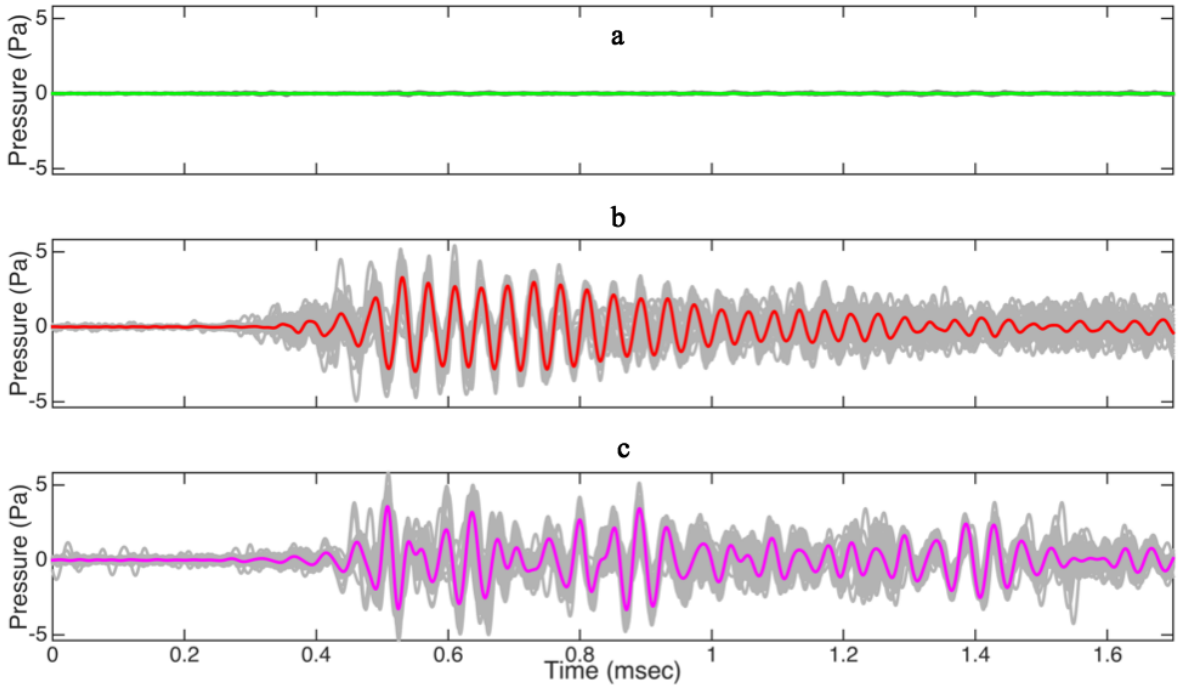

Figure 4-19: a) extracted response of the non-defected lifting weight; b) Extracted response of the lifting weight with the synthetic defect #1; c) Extracted response of the lifting weight with the synthetic defect #2

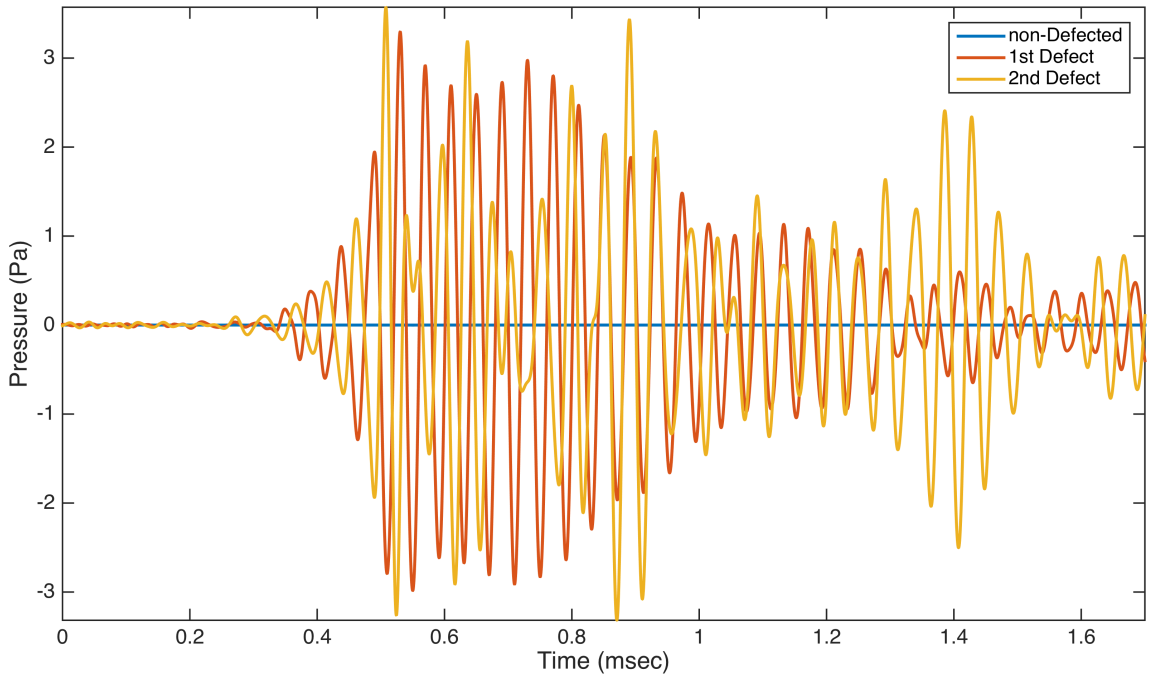

Figure 4-20: extracted responses of the non-defected lifting weight, lifting weight with synthetic defect #1, lifting weight with synthetic defect #2

4.8 Isolating the Signature Response of Defects in Time Domain

As mentioned before by each impact of the hammer, there is more than one path for emitting the wave through the structure and air, which each of them has particular arrival time to the microphone (Figure 4-21). Thus, each run interrupted by a lot of echoes that makes recognizing the pure signature response difficult. In the other words, all the extracted signature response is not the real response of the defect.

In the calibration step, the microphone is located in closest distance to the defect, to get the defect response, as well as increase the SNR. So, the propagated defect response is the first received response by the microphone, and by defining a window in the time domain, the real signature response of each defect could be isolated. Figure 4-22, illustrates a simple multipath propagation model in the longitudinal beam. Three paths were defined: 1) Path A or structure-borne path, when

the beam is hit in the one the end, pressure waves goes through the beam, reach to the defect and part of them emit to the air (Equation (4-19)); 2) Path B, another part of the waves continue and go to the other end of the beam and back to the defect and again part of them emit to the air(Equation (4-20)); 3) Path C or airborne path, after hitting the structure, part of the waves emit through the air to reach the microphone (Equation (4-21)). The Airborne path does not include any data from the defect and the emissions from this path are among the data, desired to be omitted.

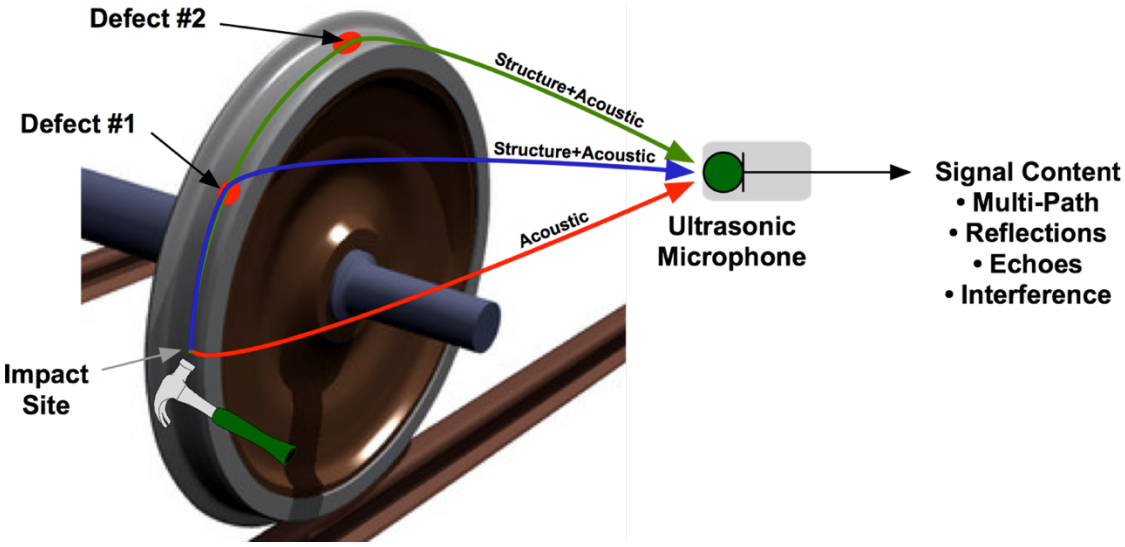

Figure 4-21: Multipath wave emission in a rail-wheel

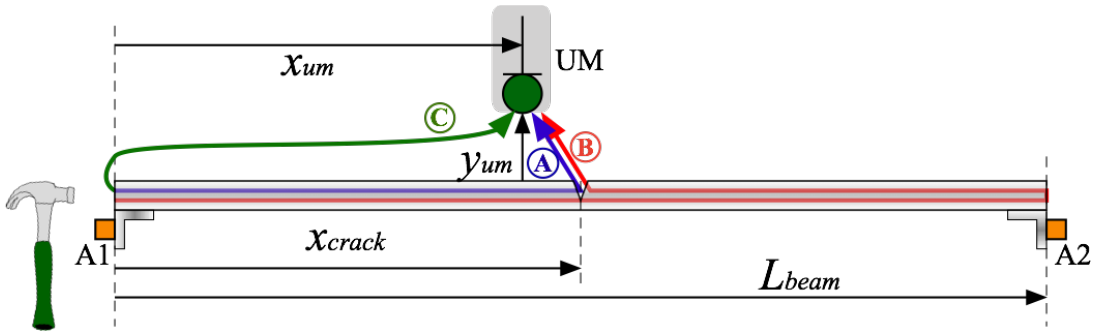

Figure 4-22: Wave propagation paths for a longitudinal beam

$$T_{arrival}^{path\ A} \approx \left(\frac{x_{crack}}{v_{alum}}\right) + \left(\frac{\sqrt{(x_{crack} - x_{um})^2 - y_{um}^2}}{v_{air}}\right) \quad 4\text{-}19$$

$$T_{arrival}^{path\ B} \approx \left(\frac{2L_{beam} - x_{crack}}{v_{alum}}\right) + \left(\frac{\sqrt{(x_{crack} - x_{um})^2 - y_{um}^2}}{v_{air}}\right) \quad 4\text{-}20$$

$$T_{arrival}^{path\ C} \approx \left(\frac{\sqrt{x_{um}^2 - y_{um}^2}}{v_{air}}\right) \quad 4\text{-}21$$

Where in Equation (4-19 to 4-21), x_{crack} is the longitudinal location of the defects, x_{um} and y_{um} are respectively longitudinal and horizontal positions of the ultrasonic microphone, L_{beam}, is the length of the beam. v_{air} and v_{alum} are respectively the speed of sound in air and aluminum. The time distance between the first and second received emissions by the microphone (Path A and Path B), is the period, when the response of the defect did not interrupt by echoes, so the pure response of each defect by isolating the signature response between these arrival times, the pure signature of each defect could be calculated. Arrival times for these three paths were calculated by using the experiment specification for the beam experimental setup (Table 4-2).

The window is calculated for the beam experiment, and as Figure (4-23) shows all the response of the defect is not the signature response of the defect, and only the highlighted section is the pure response of the defect.

Table 4-2: Longitudinal beam experimental setup character

L_{beam}	2.24 m
x_{um}	1.12 m
x_{crack}	1.12 m
y_{um}	0.025 m
v_{alum}	5200 $^{m}/_{s}$
v_{air}	345 $^{m}/_{s}$

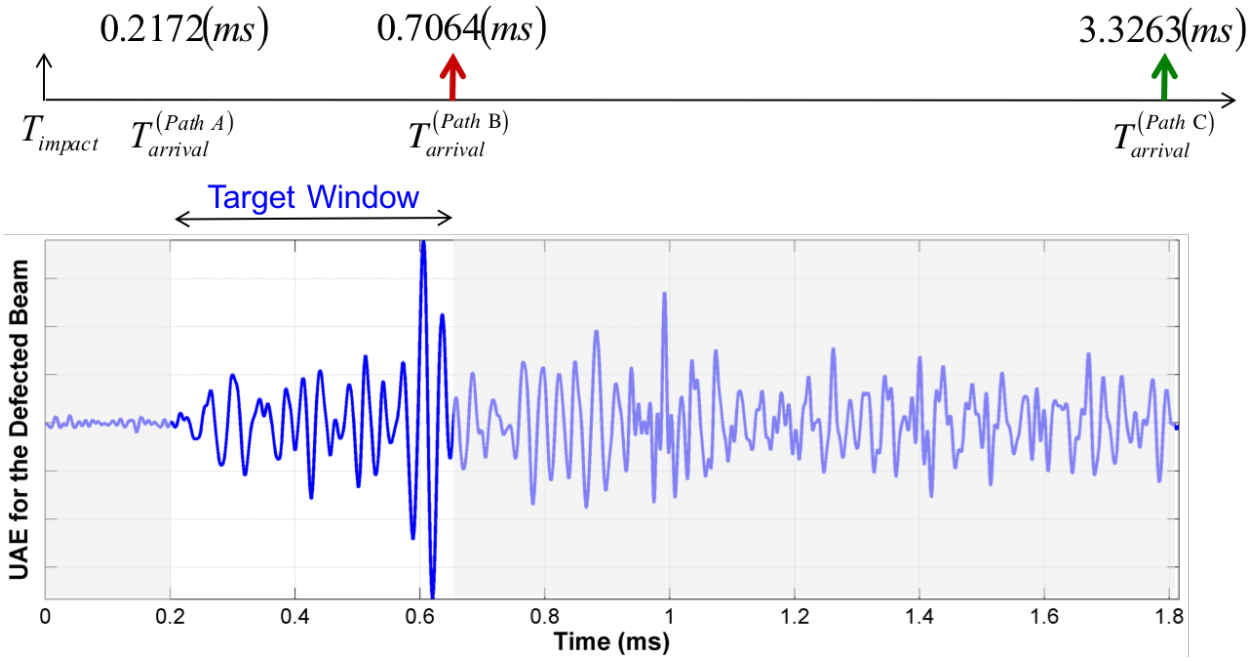

Figure 4-23: Isolating the signature response in the time domain

5 CLASSIFICATION OF DEFECTS

As Figure 5-1 illustrates, the proposal method consists of two parts. The first part is extracting the signature response of defects, as it was explained in chapter 4, and the second part is to define a method for finding the similarity between any other signal and the defect signature.

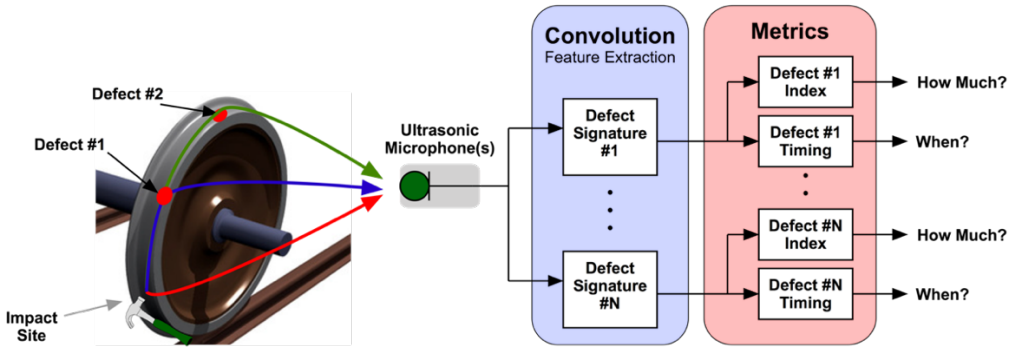

Figure 5-1: Two-steps correlation based detection system

5.1 Correlation Similarity Finding

After extracting the signature response of the defect, a correlation based method was developed to recognize the similarity of each random individual response defect to the signature response. A metric, based on the results of the cross-correlation between a run and the signature response, was defined to detect and interpret the defect type.

At the first step, cross-correlation of extracted signature response and one random run from a defected structure was calculated. To calculate the cross-correlation, the absolute value of the random signal was used (Equation 5-1)

$$\rho_{U^i_{raw}(t)\widehat{U}^n_{sig}(t)}(\tau) \equiv E\left[\left|U^i_{raw}(t)\right|\widehat{U}^n_{sig}(t-\tau)\right] \qquad 5\text{-}1$$

By using the Cauchy-Schwarz inequality formula and Equation (5-2)

$$\begin{aligned}\left|U_{raw}^{i}(t)\right| &= \left|U_{sig}^{i}(t+\Delta_i) + U_{inband}^{i}(t) + U_{oob}^{i}(t)\right| \\ &\leq \left|U_{sig}^{i}(t+\Delta_i)\right| + \left|U_{inband}^{i}(t)\right| + \left|U_{oob}^{i}(t)\right|\end{aligned} \quad 5\text{-}2$$

By replacing the Equation (5-2) into the Equation (5-1)

$$\rho_{U_{raw}^{i}(t)\widehat{U}_{sig}^{n}(t)}(\tau) = E\left[\widehat{U}_{sig}^{n}(t-\tau)\left|U_{raw}^{i}(t)\right|\right] + 0 + 0 \quad 5\text{-}3$$

The reason that the absolute value of the signal was used above is the fact that sometimes the signature response and the random runs have good correlation, but its value is negative. Thus, the absolute value of the random signal was used in this study to prevent this problem.

After finding the similarity between each random runs and signature response, it necessary that a metric is defined to recognize that how much of each defect exists in each run. Different metrics were defined and tested for this purpose. At the end using the crest factor of the cross-correlation between the signature response and the absolute value of the random run was chosen because of its better and more reliable results [11]. The final metric is defined, based on finding the sharpness of the correlation results, because the large and sharp peaks stand out from the background and they typically exhibit good correlation.

Equation (5-4) shows the metric.

$$CF = \frac{\max\left(\rho_{U_{raw},U_{sig}}\right)}{rms\left(\rho_{U_{raw},U_{sig}}\right)} - offset \quad 5\text{-}4$$

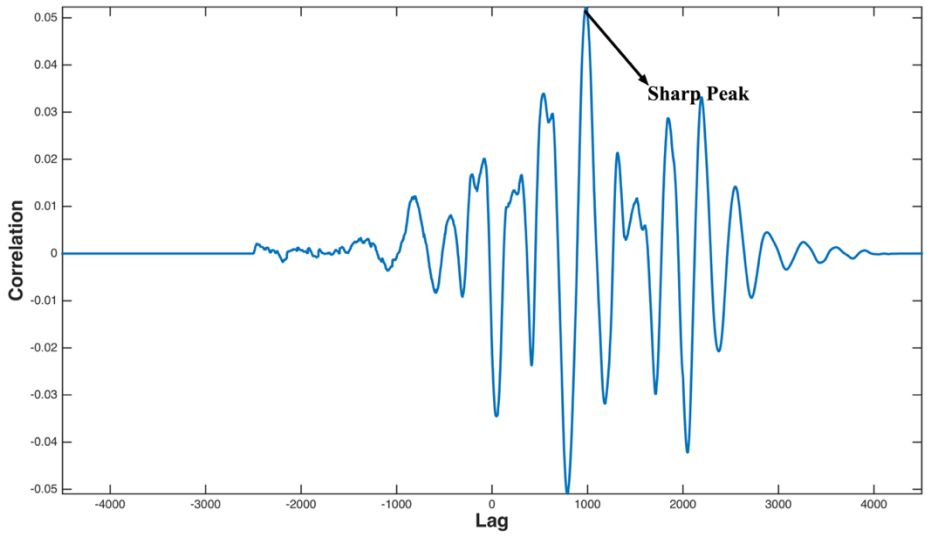

Figure 5-2: Example of cross-correlation result and finding the sharp peaks

where, value of the offset is different for each signature and defect due to the difference in the peak and mean values of the cross correlation between each defect and signature, which in this study the values of the offset is equal to the maximum value of the CF of the cross-correlation of the non-defected runs and the defect signature.

$$offset_i = \max\left(\frac{\max\left(\rho_{U_{sig}^i, U_{sig}^i}\right)}{rms\left(\rho_{U_{sig}^i, U_{sig}^i}\right)}\right) \qquad 5\text{-}5$$

where, $U_{ND}(t)$ is the raw ultrasonic response of a non-defected structure, and U_{sig}^i(t) is the signature of a certain defect.

5.2 Detecting Defects on the Lifting Weight

As mentioned earlier this study was about extracting the signature response of defects and using them to find the same type of defect on the other structures. The signature response of defects was extracted successfully in the previous part. In this part, it was tied to detect the same defect in the structure by using some random runs from the structure.

Next, the metric was used to detect or reject the existence of different types of defects on the lifting weight. At the first try, the first signature was used to detect the synthesized defect #1 on the lifting weight. Four cases were considered for this experiment: 1) microphone at the radial location and no defect, 2) microphone at radial location and defect at 0 degrees, 3) microphone at axial location and defect at 90 degrees, 4) microphone at radial location and defect at 90 degrees. Due to the reason that the offset was defined as the maximum value of the metric for the non-defected runs, so if runs do not include any defect same as the used signature response, the value of the metric for them should be negative, and if they include any defect response in them the value of their metric should be positive. As the results indicate, at this case all the defect were recognized by the metric successfully (Figure5-6). Although, only one individual rum can be used for detecting process, using more runs and calculating their average (flat line in each Figure 5-6 to 5-9) would improve the accuracy of the detection.

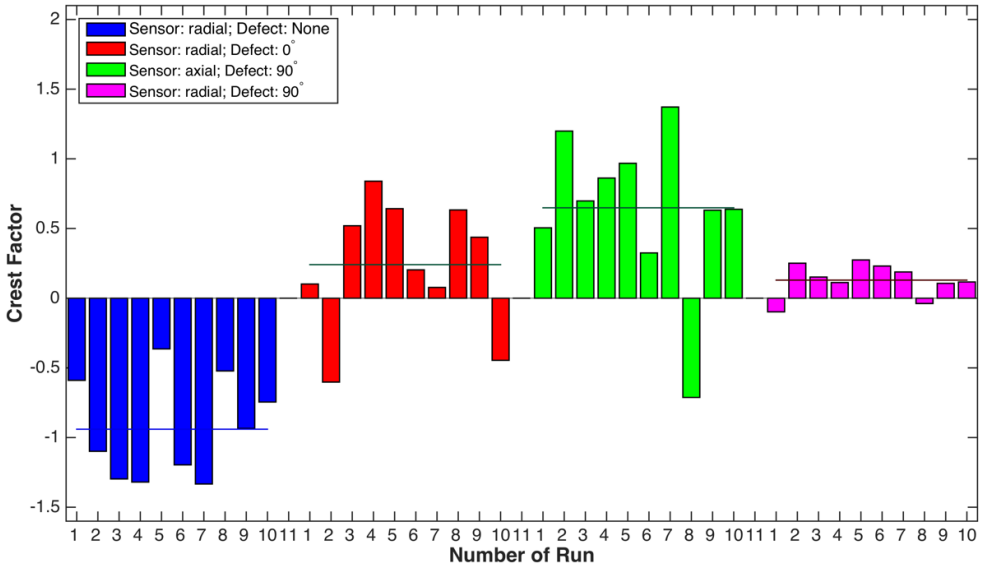

Figure 5-3: Applying the metric for detecting the defects for defect #1 by using the 1st signature. The flat lines indicate the average of CF value in each case.

As the Figure 5-14 indicates, cross-correlation for each defect and signature was calculated, and the CF value of them was calculated. As the plot shows although, in most cases even by a single run existence of the defect in the structure could be or be rejected, having more runs could have improved the average and give a more accurate result.

In the next step, again the signature from defect 1 was used, and the metric was calculated again for them. As the results in Figure 5-7 indicate, the metric value for most of the cases is negative which successfully show that the synthesized defect #2 response was not on the data.

The two above process were repeated with signature #2 again. Figure 5-8, shows the metric value while the second metric was used for the first synthesized defect. Except the case that the sensor was 7 in., away from the structure, other results clearly show that the metric results show the second defect did not use in this case.

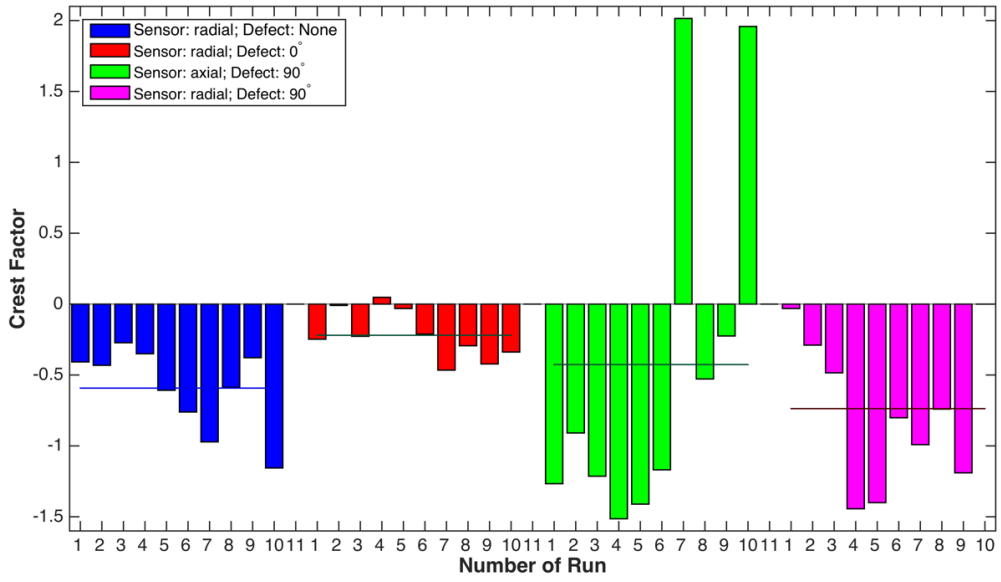

Figure 5-4: Applying the metric for detecting the defects for defect #1 by using the 2nd signature.

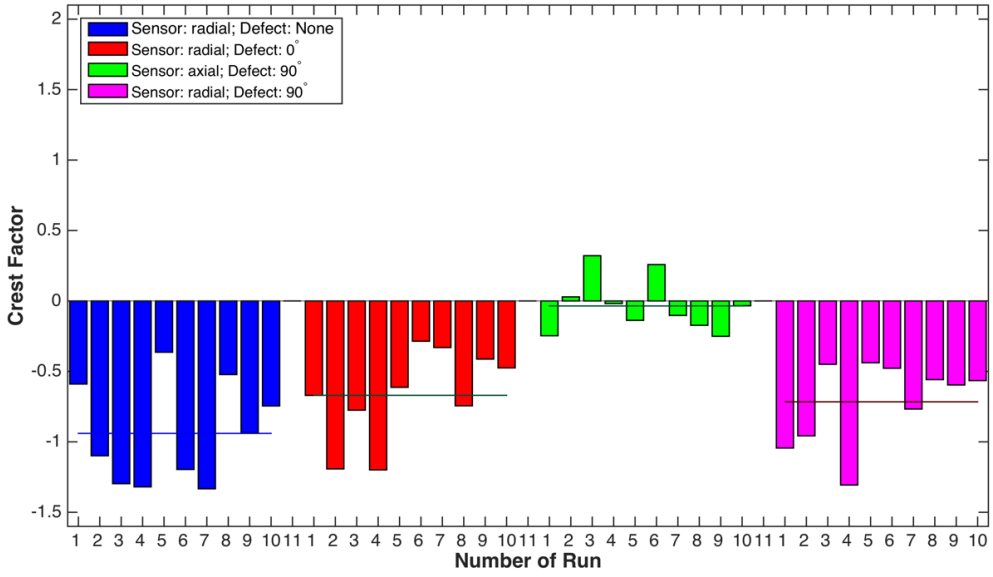

Figure 5-5: Applying the metric for detecting the defects for defect #2 by using the 1st signature.

In the last case, the second signature used to detect the second defect on the lifting weight. The metric successfully predicts the existence of the defect in the structure, except in one case that the location of the defect was changed to 90 degrees (Figure 5-6).

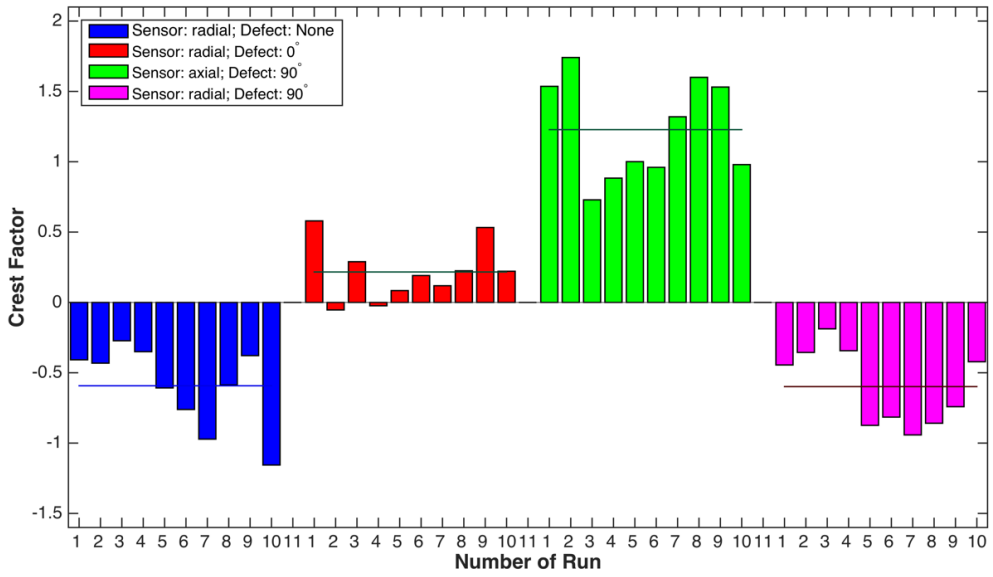

Figure 5-6: Applying the metric for detecting the defects for defect #2 by using the 2nd signature.

5.3 Detecting Defects on the Rail Wheel

In the next step, the extracted signature from the lifting weight were used to detect the same type of the defect on the defect on the rail wheel. Three cases were considered: 1) microphone at the radial location and no defect, 2) microphone at radial location and defect #1 at 0 degrees, 3) microphone at radial location and defect #2 at 0 degrees. The metric was calculated for each group of runs, once by using the signature response of defect #1 (Figure 5-7), and another time by by using the signature response of the second defect (Figure 5-8).

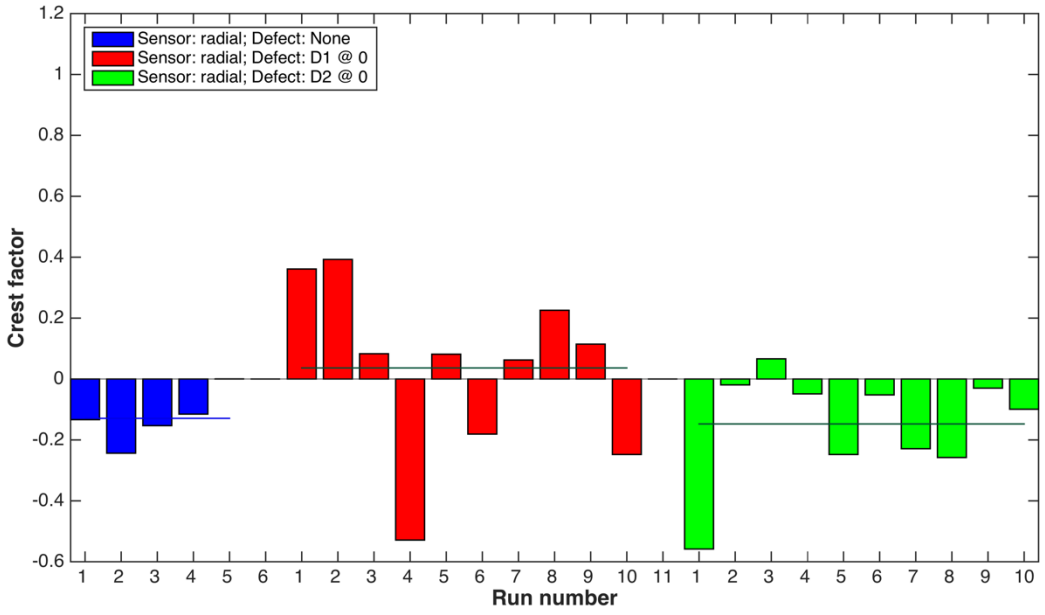

Figure 5-7: Applying the metric for detecting the defects on the rail wheel by using the signature response of defect #1

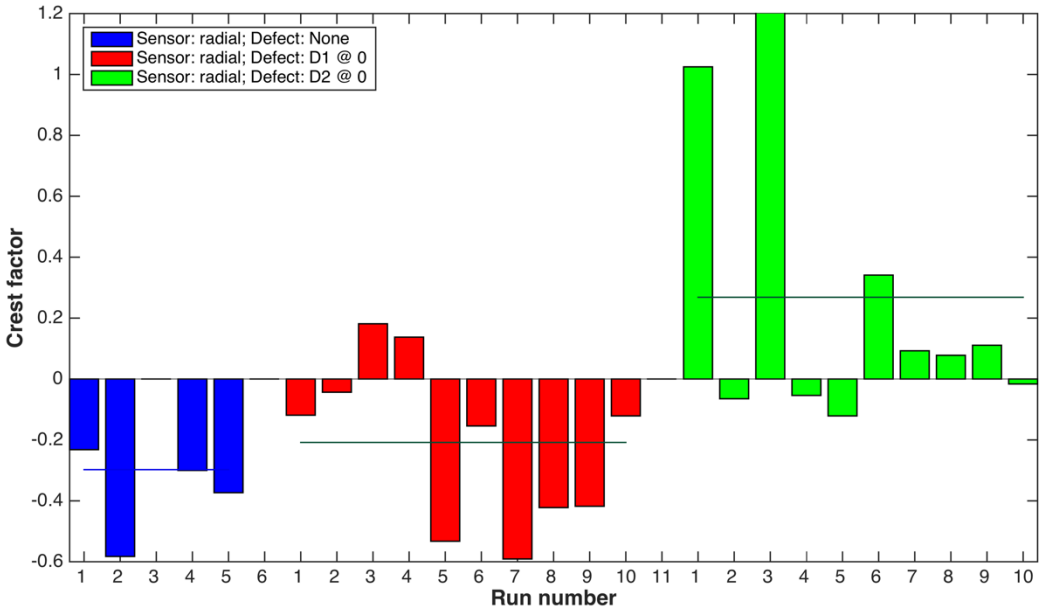

Figure 5-8: Applying the metric for detecting the defects on the rail wheel by using the signature response of defect #2

As the results indicate, in both cases the the metric successfully detected the non-defected wheel, and it predicts the first defect and rejects the second defect clearly.

6 CONCLUSION

The emitted ultrasound energy was analyzed for two structures, and a two-step method was developed for defect detection in a beam and the lifting weight in a controlled lab experiment, which the experimental setup for the beam was designed for a better understanding of the physics of the wave propagation. In the first step of this process, the signature response of each defect was de-noised and extracted. Then, a convolution-based method was defined to classify the defects. Also, a metric was proposed, based on the correlation result sharpness for identifying the content of the defect in the structure. This metric was evaluated in an experimental case study using a lifting weight. Two different synthesized defects were defined on the lifting weight, and the results confirmed that the proposed metric is able to detect and classify the defects using data from only a single impulsive excitation; however, the reliability of the prediction is shown to increase with each additional batch of data. Also, the extracted features from the defects on the lifting weight were used to detect the same type of defects on the actual rail-wheel that the defects were successfully detected by the metric.

REFERENCES

[1] R. T. Anderson, "Quantitative Analysis of Factors Affecting Railroad Accident Probability and Severity," p. 110, 2005.

[2] X. Liu, M. R. Saat, and C. P. L. Barkan, "Analysis of causes of major train derailment and their effect on accident rates," *Transp. Res. Rec.*, vol. 2289, no. 2289, pp. 154–163, 2012.

[3] P. E. Mix, *Introduction to nondestructive testing: a training guide*, John Wiley. 2005.

[4] S. Sundararaman, *Numerical and experimental investigations of practical issues in the use of wave propagation for damage identification*. ProQuest, 2007.

[5] D. . McCann and M. . Forde, "Review of NDT methods in the assessment of concrete and masonry structures," *NDT E Int.*, vol. 34, no. 2, pp. 71–84, 2001.

[6] J. Blitz and G. Simpson, *Ultrasonic methods of non-destructive testing*, vol. 2. Springer Science & Business Media, 1995.

[7] R. E. Green, "Noncontact acoustical techniques for nondestructive characterization of materials and structures," *Int. Appl. Mech.*, vol. 38, no. 3, pp. 253–259, 2002.

[8] J. Chen, Y. Shi, and S. Shi, "Noise analysis of digital ultrasonic nondestructive evaluation system," *Int. J. Press. Vessel. Pip.*, vol. 76, no. 9, pp. 619–630, 1999.

[9] A. Sinclair, "Analysis of the ultrasonic frequency response for flaw detection: A technical review," *Mater. Eval.*, vol. 43, no. 1, pp. 105–107, 1985.

[10] D. W. Fitting and L. Adler, *Ultrasonic spectral analysis for nondestructive evaluation*. Plenum Publishing Corporation, 1981.

[11] B. V. K. V. Kumar, A. Mahalanobis, and R. D. Juday, *Correlation pattern recognition*. Cambridge University Press, 2005.

[12] D.-M. Tsai and C.-T. Lin, "Fast normalized cross correlation for defect detection," *Pattern Recognit. Lett.*, vol. 24, no. 15, pp. 2625–2631, 2003.

[13] J. Ooi and K. Rao, "New insights into correlation-based template matching," in *Orlando'91, Orlando, FL*, 1991, pp. 740–751.

[14] R. Brunelli and T. Poggio, "Face recognition: Features versus templates," *IEEE Trans. Pattern Anal. Mach. Intell.*, no. 10, pp. 1042–1052, 1993.

[15] J. H. Kim, H. S. Cho, and S. Kim, "Pattern classification of solder joint images using a correlation neural network," *Eng. Appl. Artif. Intell.*, vol. 9, no. 6, pp. 655–669, 1996.

[16] "www.avisoft.com," 2014. [Online]. Available: http://www.avisoft.com/usg/cm16_cmpa.htm. [Accessed: 03-Mar-2016].

[17] P. Cawley and R. D. Adams, "The location of defects in structures from measurements of natural frequencies," *J. Strain Anal. Eng. Des.*, vol. 14, no. 2, pp. 49–57, 1979.

[18] S. W. Doebling, C. R. Farrar, M. B. Prime, and D. W. Shevitz, "A review of damage identification methods that examine changes in dynamic properties," *Shock Vib. Dig.*, vol. 30, no. 2, pp. 91–105, 1998.

[19] C. R. Farrar and H. Y. Sohn, "Condition/damage monitoring methodologies.," 2001.

[20] I. Solodov, D. Döring, and G. Busse, "New opportunities for NDT using non-linear interaction of elastic waves with defects," *Strojni{š}ki vestnik-Journal Mech. Eng.*, vol. 57, no. 3, pp. 169–182, 2011.

[21] I. Solodov, “Nonlinear Acoustic Ndt : Approaches , Methods , and Applications,” *10th Int. Conf. Slov. Soc. Non-destructive Test.*, pp. 1–16, 2009.

[22] C. H. Knapp and G. C. Carter, “The generalized correlation method for estimation of time delay,” *Acoust. Speech Signal Process. IEEE Trans.*, vol. 24, no. 4, pp. 320–327, 1976.

[23] A. Gaouda and M. Salama, “Power quality detection and classification using wavelet-multiresolution signal decomposition,” *Power Deliv. IEEE ...*, vol. 14, no. 4, pp. 1469–1476, 1999.

[24] A. H. Nuttall, G. C. Carter, and E. M. Montavon, “Estimation of the two-dimensional spectrum of the space-time noise field for a sparse line array,” *J. Acoust. Soc. Am.*, vol. 55, no. 5, pp. 1034–1041, 1974.

[25] R. Ott and M. Longnecker, *An introduction to statistical methods and data analysis*. Cengage Learning, 2008.

[26] D. S. Moore, G. P. McCabe, and B. A. Craig, “Introduction to the Practice of Statistics,” 2012.